Geochemistry Geophysics Geosystems G3

Article
Volume 14, Number 12
20 December 2013
doi: 10.1002/2013GC004858
ISSN: 1525-2027

Published by AGU and the Geochemical Society

Seafloor photo-geology and sonar terrain modeling at the 9°N overlapping spreading center, East Pacific Rise

Emily M. Klein
Nicholas School of the Environment, Duke University, Box 90227, Durham, North Carolina, 27708, USA (ek4@duke.edu)

Scott M. White
Department of Earth and Ocean Sciences, University of South Carolina, Columbia, South Carolina, USA

James Andrew Nunnery
Nicholas School of the Environment, Duke University, Durham, North Carolina, USA

Now at Kleinfelder, Austin, Texas, USA

Jessica L. Mason-Stack
Department of Earth and Ocean Sciences, University of South Carolina, Columbia, South Carolina, USA

Now at POWER Engineers, Lakewood, Colorado, USA

V. Dorsey Wanless
Department of Geology and Geophysics, Woods Hole Oceanographic Institution, Woods Hole, Massachusetts, USA

Michael R. Perfit
Department of Geological Sciences, University of Florida, Gainesville, Florida, USA

Christopher L. Waters
Geosciences Research Division, Scripps Institution of Oceanography, University of California San Diego, La Jolla, California, USA

Kenneth W. W. Sims
Department of Geology and Geophysics, University of Wyoming, Laramie, Wyoming, USA

Daniel J. Fornari
Department of Geology and Geophysics, Woods Hole Oceanographic Institution, Woods Hole, Massachusetts, USA

Anne J. Zaino
Nicholas School of the Environment, Duke University, Durham, North Carolina, USA

Now at Institute of Earth Science and Engineering, University of Auckland, Auckland, New Zealand

W. Ian Ridley
USGS, Mineral Resources Program, Denver Federal Center, Denver, Colorado, USA

[1] A fundamental goal in the study of mid-ocean ridges is to understand the relationship between the distribution of melt at depth and seafloor features. Building on geophysical information on subsurface melt at the 9°N overlapping spreading center on the East Pacific Rise, we use terrain modeling (DSL-120A side scan and bathymetry), photo-geology (Jason II and WHOI TowCam), and geochemical data to explore this relationship. Terrain modeling identified four distinct geomorphic provinces with common seafloor characteristics that correspond well to changes in subsurface melt distribution. Visual observations were used to interpret terrain modeling results and to establish a relative seafloor age scale, calibrated with radiometric age dates, to identify areas of recent volcanism. On the east limb, recent eruptions in the north are localized over the margins of the 4 km wide asymmetric melt sill, forming a prominent off-axis pillow ridge. Along the southern east limb, recent eruptions occur along a neovolcanic ridge that hugs the overlap basin and lies several kilometers west of the plunging melt sill. Our results suggest that long-term southward migration of the east limb occurs through a series of diking events with a net southward propagation direction. Examining sites of recent eruptions in the context of geophysical data on melt distribution in the crust and upper mantle suggests melt may follow complex paths from depth to the surface. Overall, our findings emphasize the value of integrating information obtained from photo-geology, terrain modeling, lava geochemistry and petrography, and geophysics to constrain the nature of melt delivery at mid-ocean ridges.

Components: 13,950 words, 12 figures.

Keywords: mid-ocean ridge; overlapping spreading center; melt lens; axial magma chamber; dike; ocean crust.

Index Terms: 3035 Midocean ridge processes: Marine Geology and Geophysics; 3045 Seafloor morphology, geology, and geophysics: Marine Geology and Geophysics; 3040 Plate tectonics: Marine Geology and Geophysics; 8150 Plate boundary: general: Tectonophysics; 8155 Plate motions: general: Tectonophysics; 8157 Plate motions: past: Tectonophysics; 8158 Plate motions: present and recent: Tectonophysics; 1032 Mid-oceanic ridge processes: Geochemistry; 1036 Magma chamber processes: Geochemistry; 3614 Mid-oceanic ridge processes: Mineralogy and Petrology; 3618 Magma chamber processes: Mineralogy and Petrology; 8416 Mid-oceanic ridge processes: Volcanology.

Received 13 June 2013; **Revised** 7 October 2013; **Accepted** 7 October 2013; **Published** 20 December 2013.

Klein, E. M., et al. (2013), Seafloor photo-geology and sonar terrain modeling at the 9°N overlapping spreading center, East Pacific Rise, *Geochem. Geophys. Geosyst.*, *14*, 5146–5170, doi:10.1002/2013GC004858.

1. Introduction

[2] An overarching goal in the study of mid-ocean ridges is to understand the linkages in the magmatic system from melt generation in the mantle to eruption on the seafloor. A key part of this system is the relationship between volcanism and the distribution of melt at depth in the crust and upper mantle. Axial magma lenses have been imaged by seismology beneath nearly all fast to intermediate-spreading ridges [e.g., *Detrick et al*., 1987, 2002; *Baran et al*., 2005; *Carbotte et al*., 2006] and a few slow spreading ridges [e.g., *Singh et al*., 2006]. Sheeted dike units, representing the solidified conduits that transport magma from the melt lens, are observed ubiquitously underlying the volcanic layer in tectonic windows and drill cores in fast-spread crust [*Karson*, 2002]. Thus, we know that dike intrusion is the fundamental process that brings melt from depth to erupt on the ocean floor. However, the relationships between crustal magma storage, melt transport through diking, and seafloor eruptions are not fully understood.

[3] Much attention has focused on the vertical component of dike propagation in the construction of the ocean crust [e.g., *Perfit and Chadwick*, 1998], with persuasive evidence that vertical transport dominates in some settings [e.g., *Bergmanis et al*., 2007; *Marjanović*, 2013; *Carbotte et al*., 2013]. But studies of subaerial dike intrusion events show that dikes commonly travel tens of kilometers horizontally, often erupting far from their magma source [e.g., *Björnsson et al*., 1977; *Sigurdsson and Sparks*, 1978; *Keir et al*., 2009; *Hartley and Thordarson*, 2013]. Within this context, the goal of this study is to use our knowledge of the spatial variability of subsurface melt at the 9°03′N overlapping spreading center (hereafter 9N OSC) on the East Pacific Rise (EPR) (Figure 1) to

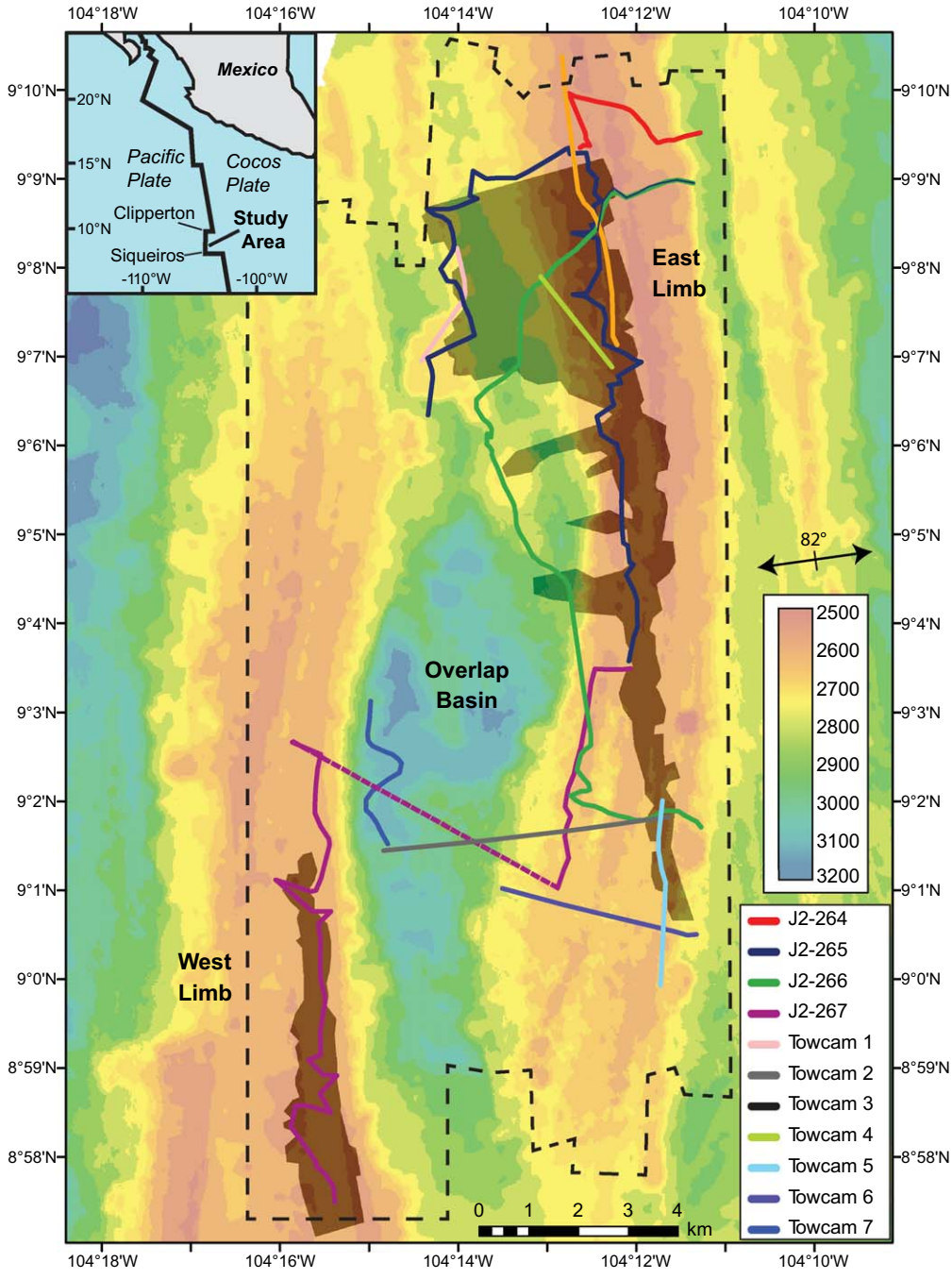

Figure 1. Bathymetric map of the 9°03′N OSC between the Clipperton and Siqueiros transform faults on the East Pacific Rise. *Jason II* and WHOI TowCam traverses are shown as colored lines (see legend). Envelope of side-scan sonar backscatter coverage, obtained along 10 north-south *DSL-120A* track lines, is shown by dashed black lines. Melt sills underlying the east and west limbs are shaded [*Kent et al*., 2000]. Spreading direction (82°) shown as black line with arrows [*Gripp and Gordon*, 2002].

characterize magma transport and associated accretion processes. The unprecedented body of geophysical data previously published for this OSC, described below, present a window into a highly variable melt supply and storage system that allows these relationships to be explored.

[4] During our 2007 R/V *Atlantis* cruise to the 9N OSC, we surveyed with *DSL-120A* side-scan sonar, and photographed and sampled seafloor using ROV *Jason II* and the WHOI TowCam. Here we report our visual and side-scan sonar results, analyzed as an integrated data set of geomorphic

seafloor observations. These data provide insights into where, when, and how the seafloor formed relative to melt distribution at depth. Results of geochemical, petrologic, magnetic, hydrothermal, and radiometric age dating studies are reported elsewhere [*Wanless et al*., 2010, 2011, 2012; *Waters et al*., 2013; *O'Brien and White*, 2007; *Zaino et al*., 2008] and are used here as complementary data that aid our interpretation of the geologic observations.

2. Background and Geologic Setting

[5] Previous bathymetric surveys of the EPR between 8°N and 10°N identified the presence of several overlapping spreading centers [*Macdonald and Fox*, 1983; *Lonsdale*, 1989], including the 9N OSC, a prominent second-order discontinuity between the Clipperton and Siqueiros transform faults (Figure 1). The 9N OSC is right stepping; its east and west limbs overlap by 27 km, with a maximum distance between the limbs of 8 km. The EPR here spreads at a full rate of ~110 mm/yr at ~N82°E, and the OSC has migrated southward at an average of ~42 mm/yr over the past ~2 my [*Carbotte and Macdonald*, 1992]. Previous side-scan sonar and reconnaissance photographic studies showed younger lava flows on the east limb compared to the west limb, suggesting that migration of the OSC occurs by southward propagation of the east limb into older lithosphere and on-average recession, or dying, of the west limb [*Sempere and Macdonald*, 1986a]. The spreading rate on each limb is believed to slow approaching the ridge tips, so that the spreading rate divided between the two limbs equals the full spreading rate for the EPR; however, the exact spreading rate at any point along each limb is unknown.

[6] Interpreting their side scan and photographic data, *Sempere and Macdonald* [1986a] described five tectonic provinces at the OSC: east and west ridges, east and west ridge tips, and overlap basin. Their interpretations suggest that the east and west ridge tips are characterized by both a high abundance of fissures rotated clockwise relative to the direction of Cocos-Pacific Plate spreading and increasing ridge crest depths approaching the tip. East and west ridges are characterized by an axial summit trough that becomes less well-defined approaching each ridge tip. The west ridge tip disappears to the north into the block faulted abyssal hill terrain of the western flank of the EPR. Photographs of the overlap basin suggest a volcanically dominated region characterized by large volcanic edifices with few faults or fissures. *Sempere and Macdonald* [1986a] had difficulty collecting Deep-Tow photographs due to the steep terrain everywhere except on the east and west ridges, where they found mainly old-appearing pillow lavas with a few more glassy-looking pillows along the highly fissured axes.

[7] The 9N OSC has been the focus of extensive efforts to characterize the spatial distribution and characteristics of melt at depth. Of particular interest are results of the first true three-dimensional seismic reflection survey on a mid-ocean ridge [ARAD survey of *Kent et al*., 2000] as well as a three-dimensional seismic refraction study [*Dunn et al*., 2001; *Toomey et al*., 2007]. These studies, combined with older multichannel seismic work [*Detrick et al*., 1987; *Harding et al*., 1993; *Kent et al*., 1993], provide one of the most detailed characterizations of subsurface melt distribution available for any part of the global ocean ridge system. Along the east limb, seismic reflection results [*Kent et al*., 2000; *Singh et al*., 2006; *Tong et al*., 2002] reveal a shallow (~1.6–2.2 km beneath the seafloor), asymmetric, >4 km wide melt sill, or axial magma chamber, extending westward from the east limb axis just north of the overlap basin (Figure 1). Further south along the east limb, the sill narrows to <250 m wide and plunges ~500 m in depth, cutting across the surficial ridge fabric and terminating off-axis east of the propagating limb tip. In contrast to the variable width and depth of the melt sill beneath the east limb, the sill imaged beneath the west limb is centered below the ridge axis and varies little in width or depth within the area studied [*Kent et al*., 2000]. Although no melt sill was mapped beneath the OSC basin, midcrustal [*Bazin et al*., 2003] and lower crustal [*Crawford and Webb*, 2002] melt have been identified beneath the northern part of the basin, and an upper mantle low velocity zone, suggesting a few percent melt, cuts diagonally across the basin from the west to the east limb [*Dunn et al*., 2001; *Toomey et al*., 2007].

3. Data Collection and Methods

[8] Data collection took place during the Medusa 2007 cruise from March to April 2007 aboard R/V Atlantis (AT15-17) using the ROV *Jason II*, WHOI TowCam, and the *DSL-120A* side-scan sonar system [*Klein et al*., 2007]. Data reported here are archived in the Integrated Earth Data Applications: Marine Geoscience Data system

Figure 2. Representative photographs and descriptions for each rank in the relative age scale. Photographs, available through the Jason Virtual Van system, are: Youngest: Pilot.20070406_072224, Pilot.20070412_082524; Young: Pilot.20070406_001044, 20070412_164521; Intermediate: Pilot_20070411_004441, 3Chip.20070412_013944; Old: 3Chip.20070405_230112, Pilot.20070412_002512; Oldest: 3Chip.20070412_001613, Pilot.20070405_224442.

(www.marine-geo.org/tools/search/entry.php?id=AT15–17).

[9] *Jason II* was deployed four times (Figure 2; J2–264, J2–265, J-266, J2–267) for a total of 234 h covering ~20.4 km (Figure 1). We collected ~7000 digital photographs, 213 h of three video streams, 282 rock samples, and hydrothermal vent waters and biota from the Medusa vent site. The WHOI TowCam [*Fornari*, 2003] digital camera system was deployed seven times, collecting ~10,000 photographs (Figure 1). TowCam photographs were time-stamped and geo-referenced using layback-calculated position of TowCam from the ship's position, course, and wire out.

[10] *DSL-120A* is a 120 kHz phase bathymetric side-scan sonar system with a near-nadir backscatter pixel resolution of ~1 m and ~4 m for bathymetry when flown 100–125 m above the seafloor [*Scheirer et al.*, 2000]. Ten track lines were used to achieve 100% backscatter coverage within the mapped area to closely match the ARAD seismic survey region (Figure 1). Navigation was initially

determined by layback positioning from the GPS position of the R/V Atlantis, and then manually adjusted after the survey by matching features on overlapping swaths. Comparison of distinctive features in the *DSL-120A* with EM300 bathymetry [*White et al*., 2009] shows no discernable offsets. Comparison of the navigation of *DSL-120A* with *Jason II* shows excellent agreement, within 50 m and usually <10 m.

4. Seafloor Visual Observations

4.1. Relative Seafloor Age Scale

[11] Because the primary goal of our study is to explore the spatial relationships between seafloor magmatism and the distribution of melt at depth, our analysis focuses on the use of photographs to estimate seafloor age and identify sites of recent eruptions. A number of previous studies have used visual characteristics of the seafloor to estimate relative age [*Ballard et al*., 1981; *Macdonald et al*., 1988; *Embley and Chadwick*, 1994; *Haymon et al*., 1993] based primarily on the extent of sediment cover in each image, as well as other factors such as the presence or absence of reflective (i.e., fresh) basaltic glass. We developed a relative age ranking (RAR) seafloor age classification system (ranked 1–5) based on sediment cover, connectedness of sediment pockets, presence or absence of glass and delicate ornamentation on lava surfaces, relief, and extent of intact rock (Figure 2). Young seafloor (RAR 1) is characterized by the presence of glass, little or no sediment cover, well-defined extrusive forms, and common lava ornamentation. Old seafloor (RAR 5) exhibits heavy sediment cover and low relief, with outcrop comprising <10% of the photograph. RARs 2–4 grade between these end-members. It is worth noting that no seafloor photographed at the 9N OSC appears as young as the pristine volcanic terrain observed at areas of the EPR with known recent eruptions [e.g., 9°50'N, *Rubin et al*., 2012]. *Perfit and Chadwick* [1998] observe, however, that recently erupted lavas may not maintain their pristine appearance for much longer than ~1 year.

[12] Using our relative age scale, approximately every twentieth photograph from each *Jason II* and TowCam lowering was examined in order, and assigned a RAR. In cases where images were dark, cameras were aimed away from the seafloor, or the vehicle was in the same location for a long period of time, photographs were skipped and the next interpretable image was used.

[13] An evaluation of the validity of our relative age scale and estimates of absolute age for each age scale rank is presented in Supplement 1 in the supporting information.[1] This analysis, based on data collected north of the OSC [*Escartin et al*., 2007; *Sims et al*., 2002, 2003], reveals strong correlations between photographically determined relative age ranks and radiometric (U-Th) ages. On average, each unit increase in our relative age ranking represents an increase of ~18,000 years. This should be viewed as a rough estimate, however, particularly for young seafloor (RAR 1 and 2).

4.2. Photographic Results

[15] We summarize below our photographic results, emphasizing relative seafloor age estimates using our relative age scale, and include brief descriptions of lava morphology, deformation, and other features.

4.2.1. The East Limb

[16] The axial summit trough (AST) along the east limb contains the greatest extent of young seafloor (RAR 1) within our study area (Figures 3 and 4). Within the AST, lavas exhibit abundant fresh glass with little sediment cover. An active hydrothermal vent field located at 9°08.3′N, named the Medusa vent site for its pink jellyfish (*Stauromedusae*), is centered within the area of youngest lava on the east limb (Figure 4). Lava morphology along the east limb is dominated by roughly equal proportions of lobate and pillow lavas (with some large andesitic/dacitic pillows); sheet flows were rarely observed.

[17] Further south along the east limb, south of ~9°04′N, the youngest seafloor (RAR 1–2) is confined to a bathymetric ridge that curves southwestward adjacent to the overlap basin (Figures 3 and 4). Lava morphology here is similar to that observed to the north although pillow lavas appear to be more common than lobate flows. Notably, only old seafloor (dominantly RAR 3–5) is observed overlying the seismically imaged plunging melt sill. Indeed, much of the seafloor at the southern end of the east limb consists of faults and fissures (see sonar results below), which in map view fan out over a wide area extending east of the volcanically active bathymetric ridge.

[18] For most of the east limb region, off-axis photographs show the expected signs of increasing seafloor age with distance from the AST. There is one important exception, however. A prominent,

[1]Additional supporting information may be found in the online version of this article.

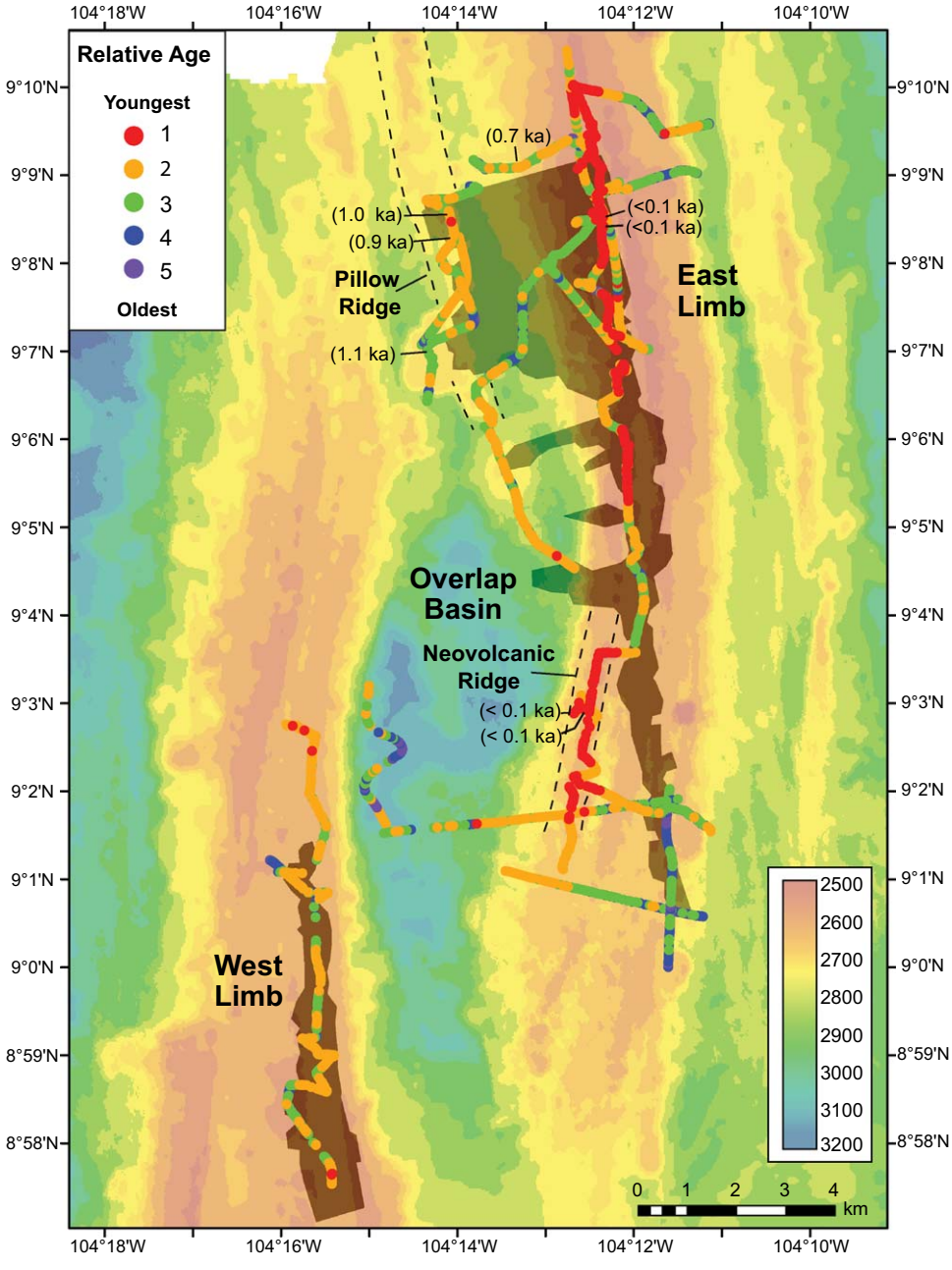

Figure 3. Relative seafloor age determined from photographic data superimposed on bathymetry. Shaded areas indicate locations of melt sills [*Kent et al*., 2000]. Youngest seafloor (1, red) to oldest seafloor (5, purple); where age symbols are superimposed, symbols for youngest relative age rank are on top. Locations of pillow ridge and neovolcanic ridge, discussed in text, are labeled. Numbers in parentheses indicate U-series model ages for samples recovered during *Jason II* dives [*Waters et al*., 2013].

pillow-dominated ridge, which overlies the western edge of the wide melt sill, was found to be anomalously young, averaging RAR of ~2, with light sediment cover, some visible glass, and delicate lava ornamentation (Figure 4). Based on crustal age calculated from spreading rate, this ridge would be expected to be ~40–68 kyr, with older RARs than observed. Following *Wanless et al*. [2012] we refer to this anomalously young feature as the "pillow ridge."

4.2.2. The West Limb

[19] Observations from the west limb are limited to a corridor <2 km wide following the ridge axis. Lava morphology consists mostly of lobate and pillow flows, with minor sheet flows. Despite the

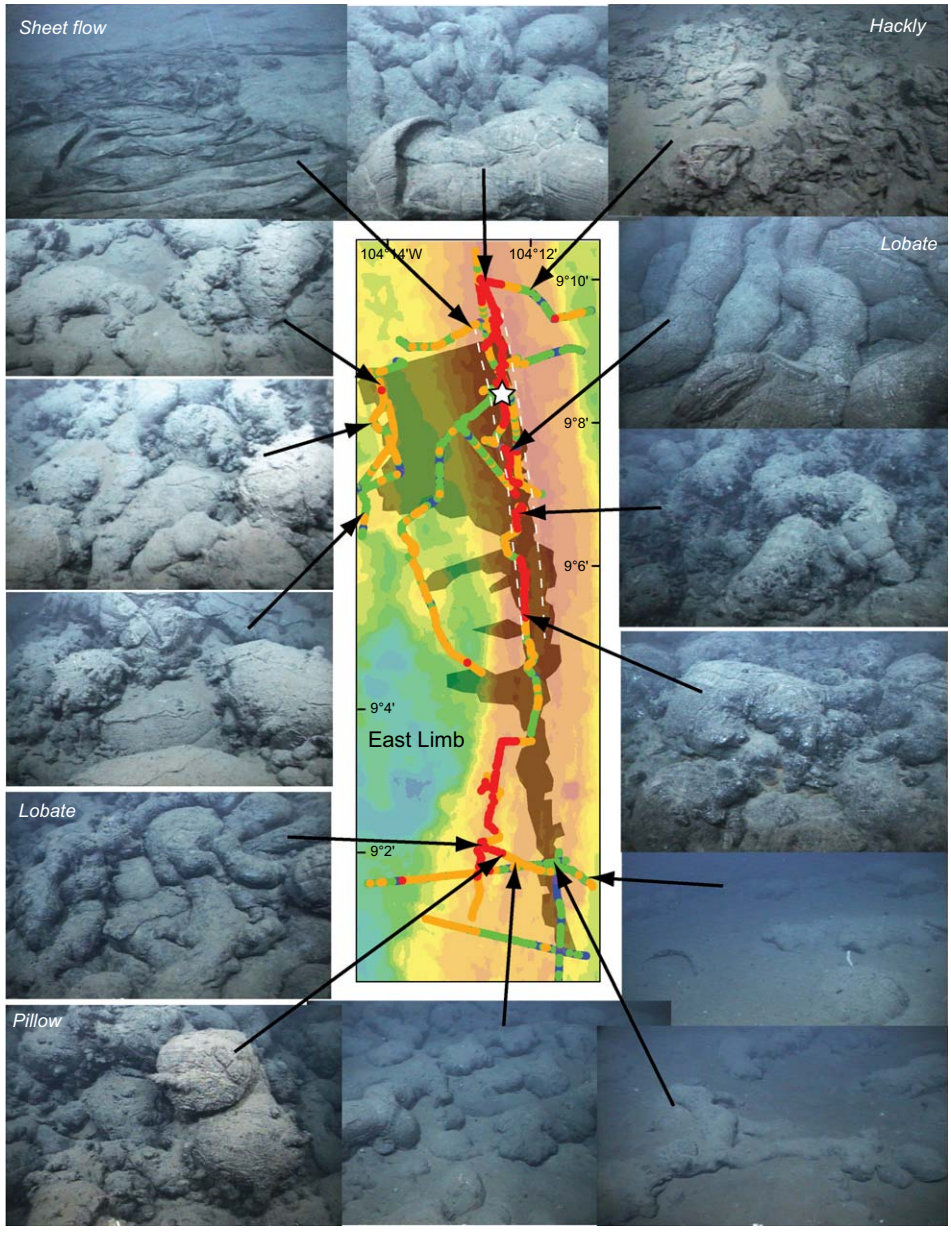

Figure 4. Representative *Jason II* photographs of seafloor along the east limb and flank, linked to detail of map from Figure 3. White star indicates location of the Medusa hydrothermal vent site. Examples of lava morphologies described in the text are labeled. Interpreted position of the axial summit trough (white dashed lines) after *Combier* [2005] and *Combier et al*. [2008].

presence of an axis-centered melt sill, seafloor ages for the west limb are typically RAR 2–3 although isolated occurrences of young seafloor (RAR 1) were also observed (Figures 3 and 5). No active hydrothermal venting or plumes were observed, although extinct hydrothermal chimneys were found. Overall, in contrast to the east limb ridge, our observations of the west limb surveyed suggest that it has experienced less frequent recent magmatic activity.

4.2.3. The Overlap Basin

[20] Photographic coverage within the overlap basin is limited to two TowCam lowerings and short transits near its edges (Figures 1, 3, and 6). A traverse extending west of the east limb tip region imaged a gradually deepening bench that consists primarily of intermediate to young seafloor (RAR 2–3) with pillow and lobate flows. Within the interior of the basin, there is a patchy distribution of young and old seafloor (RAR 2–5; Figure 6); lava

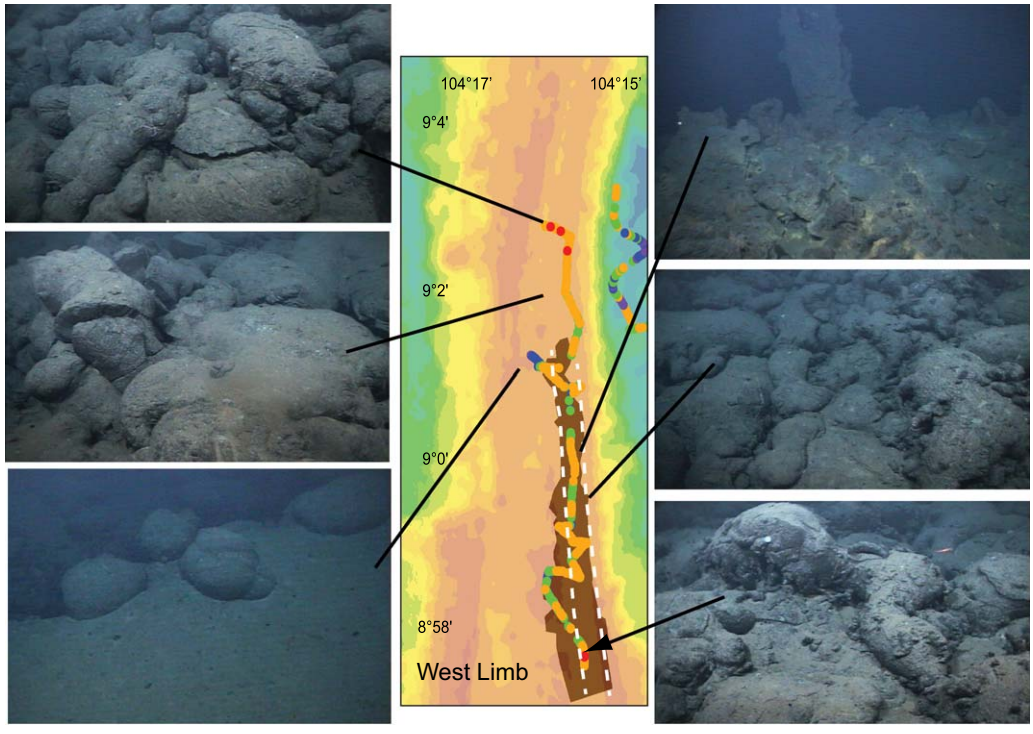

Figure 5. Representative *Jason II* photographs of seafloor along the west limb, linked to detail of map from Figure 3. Interpreted position of the axial summit trough (white dashed lines) after *Combier* [2005] and *Combier et al*. [2008].

morphology is dominated by pillows, and broken pillow fragments and talus are common. Little evidence of faulting or fissuring was observed within the basin, suggesting that infrequent eruptions repave large areas of seafloor [*White et al*., 2009] and that the basin experiences little internal deformation [*Sempere and Macdonald*, 1986a; *Tong et al*., 2005].

5. Sonar Data Analysis

[21] The *DSL-120A* sonar system collects acoustic backscatter data that provides complete seafloor imaging over a vast area of the OSC not examined visually, and thus allows us to explore variations in the characteristics of seafloor over the whole study area (Figure 7). The meter-scale resolution of the data from this system is also ideal for mapping features at the scale of individual lava flows, faults, and fissures.

5.1. Sonar-Based Classification of Seafloor

[22] Distinctive seafloor terrains were identified using a terrain modeling approach that employs objective, consistent rules to differentiate areas of different seafloor texture. We extracted patterns in seafloor texture from independent bathymetry (Supplement 2 in the supporting information) and side-scan sonar (section 3) data sets using techniques commonly employed within the field of remote sensing. It is important to note that seafloor texture is composed of volcanic, tectonic, and other features as recorded in bathymetry and side-scan sonar, and is derived independent of visual observations. Thus, while factors such as lava morphology resulting from variations in magma viscosity, local slope, and effusion rate certainly influence seafloor texture, such factors are not explicitly included in the classification.

[23] *DSL-120A* side-scan backscatter intensity was used directly along with texture patterns from gray-level co-occurrence matrices [*Haralick et al*., 1973]. For bathymetry, we merged EM300 [*White et al*., 2006], seismic seafloor reflector depth from the ARAD survey [*Combier et al*., 2008] and Hydrosweep [*Kent et al*., 2000] to create a bathymetric grid with the highest available resolution overall (30 m × 30 m; Supplement 2 in the supporting information). A grid of local relief was created, from which we derived several topographic metrics, as described in Supplement 2 in the supporting information. We ran a principal component analysis (PCA) on the side scan and topographic metrics each, to minimize the influence of redundancy in the derived raster data and reduce the computational effort of the final

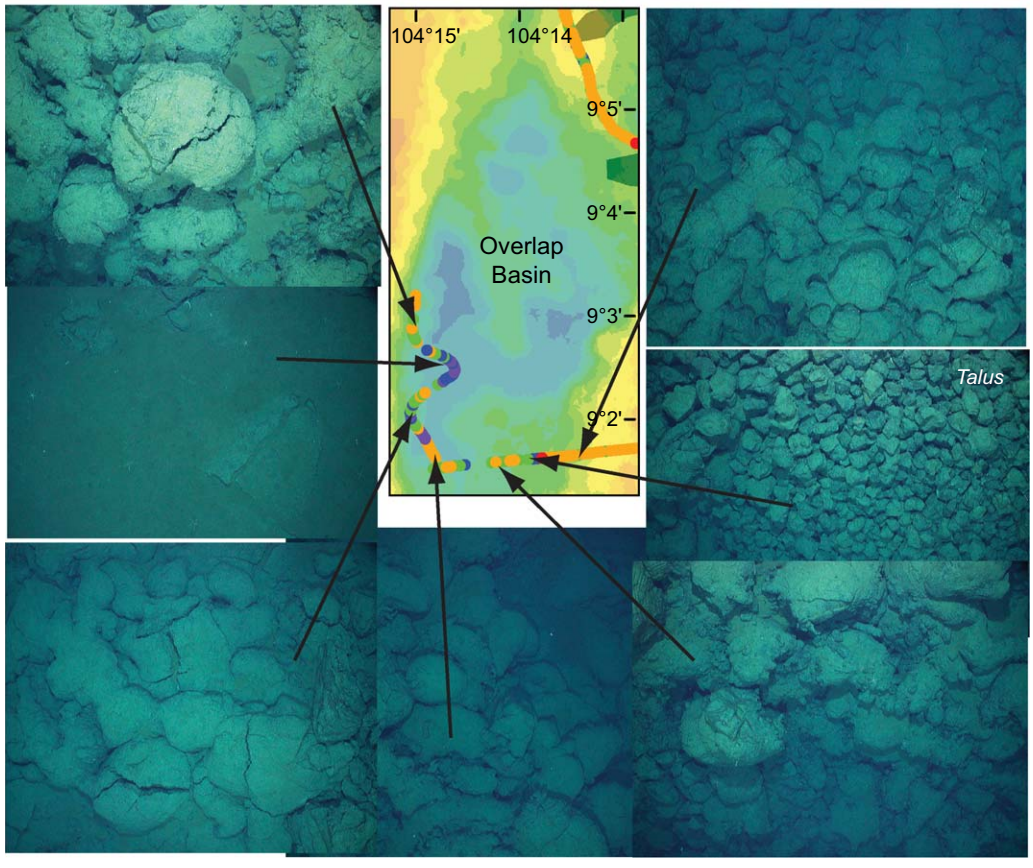

Figure 6. Representative TowCam photographs of seafloor within the overlap basin region, linked to detail of map from Figure 3. Example of talus is labeled.

classification. We then ran both a supervised and unsupervised classification using the five top PCA rasters representing >95% of the variance of the original data, to produce a classification of the unique and distinctive seafloor terrain patches present in the study area (see Supplement 3 in the supporting information for details).

[24] The identification and selection of seafloor terrains were made using both a supervised and an unsupervised classification approach (see Supplement 3 in the supporting information). In the supervised classification, an AI-classifier is trained to try to find areas where the characteristics match a known class defined by the human user [e.g., *Stewart et al.*, 1994; *Jensen*, 2005]. A supervised classification uses training data from user-select locations that best describe a particular class, to identify the distinctive characteristics of that class. The computer then uses these characteristics to assign terrain classes to every pixel in the study area. We specified five areas of interest (AOI) for the supervised classification, corresponding to the five tectonic provinces (propagating ridge, propagating tip, basin, receding ridge, receding tip) defined by *Sempere and Macdonald* [1986a]. The supervised classification found only four distinct terrains (Figure 8a), despite the five AOI (tectonic provinces) included in the supervised classification. To help confirm this result, we also performed an unsupervised classification using the ISODATA algorithm [*Ball and Hall*, 1965] (see Supplement 3 in the supporting information). In contrast to supervised classification, unsupervised classification receives no *a priori* information about what classes exist. The output represents spatial provinces with statistically distinct terrain patterns defined by the ISODATA clustering algorithm from the PCA raster stack. The unsupervised classification also produced only four classes (Figure 8b), and their spatial distribution is strikingly similar to that of the supervised classification (Figure 8a). The correspondence of these two independent techniques in identifying the number of distinct terrains and their distribution supports the validity of our terrain modeling results.

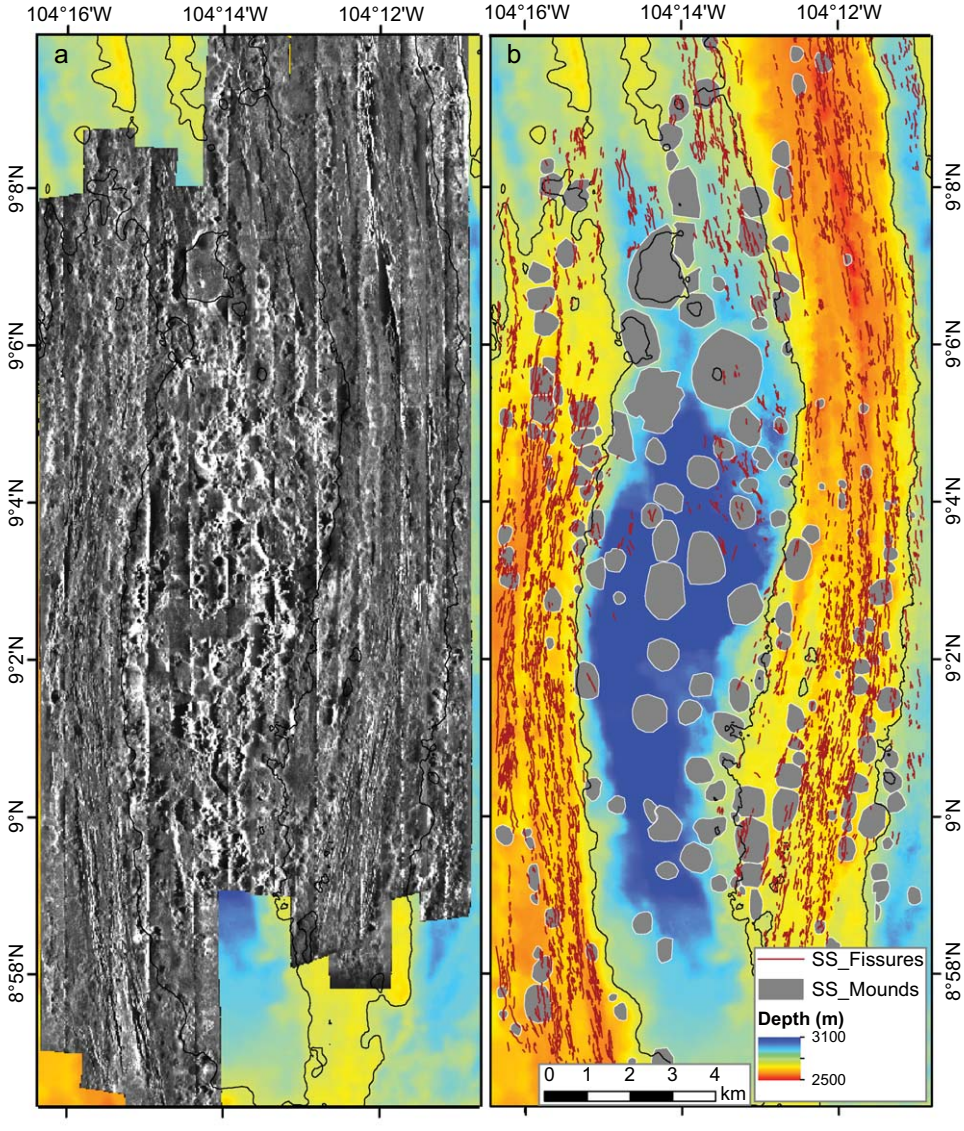

Figure 7. (a) Side-scan sonar backscatter intensity from 10 north-south-oriented *DSL-120A* track lines. Lighter areas indicate higher backscatter return, with the areas of highest return coming from steep mounds between the spreading axes. (b) Interpretations based on side scan and associated bathymetry showing mounds (gray circular features) and fissures (dark red lines). Bathymetry shown in colors (see legend) with the 2700 m depth contour (thin black lines) for reference.

[25] Our assessment of the internal consistency of the supervised classification method, described in Supplement 4 in the supporting information, indicates that the classifier consistently reproduces the classes chosen to represent distinct terrains in four out of five areas, with the fifth area identified as one of the other four. This analysis suggests that the four terrains identified are robust representations of the range of local terrain types within kilometer-scale precision. The variability in tectonic and magmatic processes that are believed to be responsible for creating different terrains are likely to vary on a similar scale [*Escartin et al*., 2007].

5.2. Sonar Classification Results: The Nature of Seafloor Within Classified Terrain Provinces

[26] Our terrain modeling suggests that similarities or differences in ocean crust construction and

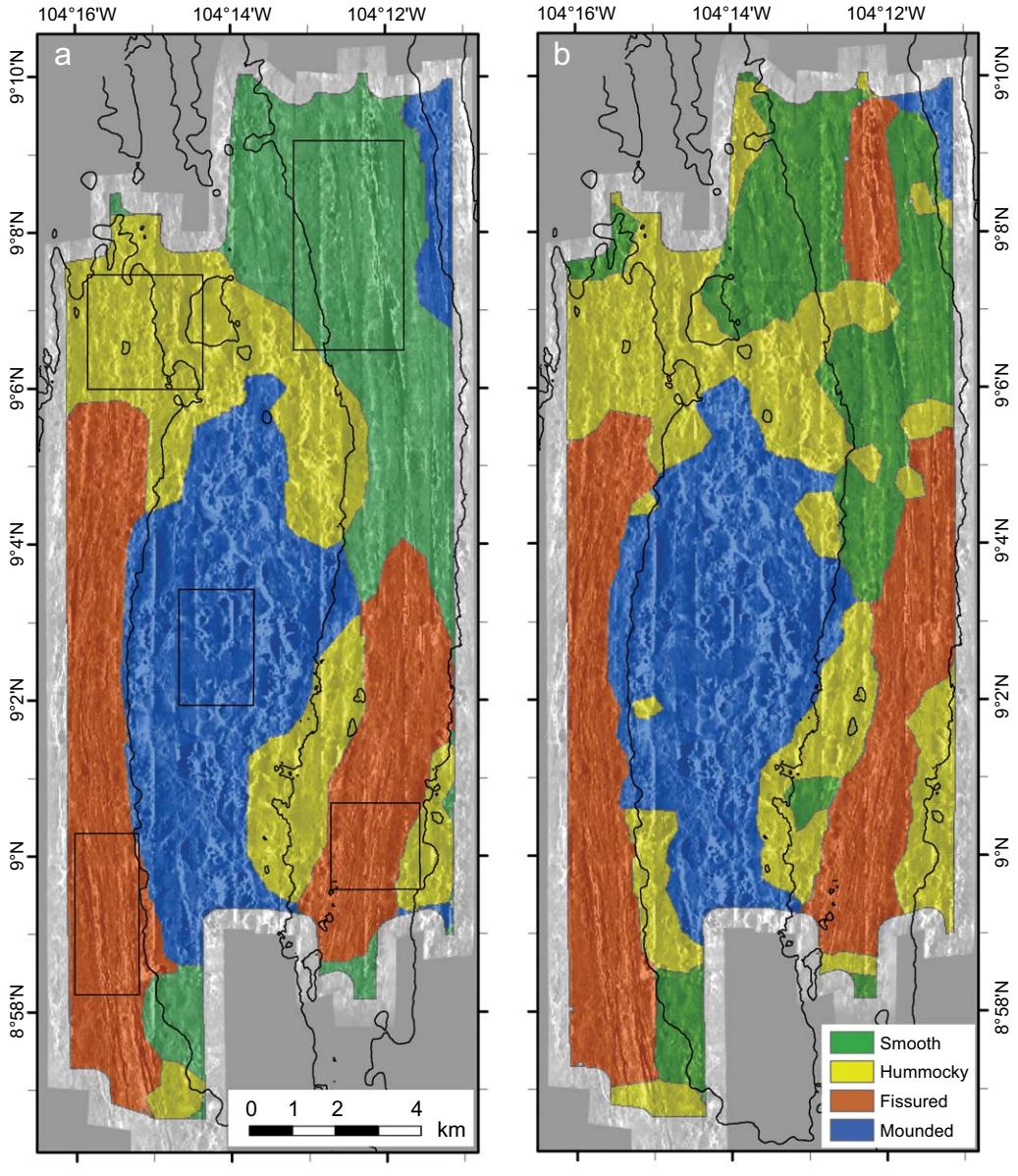

Figure 8. (a) Supervised and (b) unsupervised terrain classifications color-coded by terrain name (see legend) with shading from backscatter intensity map from *DSL-120A* (Figure 7a) and the 2700 m depth contour (black lines) for reference. (a) Results of the supervised classification; outlined boxes are the areas of interest (AOI) used in this classification and discussed in the text. (b) Results of unsupervised classification. Both classifications produce four distinct classes of seafloor terrain with similar distributions.

evolution can be meaningfully identified and explored without *a priori* assumptions of the processes that may occur in a given tectonic or geographic region (e.g., east limb, ridge tip, overlap basin). We found, for example, that the propagating "eastern ridge tip" of *Sempere and Macdonald* [1986a] contains a mix of terrains rather than a single distinct terrain.

[27] We can better understand the underlying differences that these four terrain provinces represent by examining geologic features interpreted from the sonar data (e.g., mounds, faults, fissures) as well as drawing upon the photographic data within each terrain. We manually digitized fissures, faults, mounds, and ponded lava flows from the *DSL-120A* backscatter and compiled bathymetric

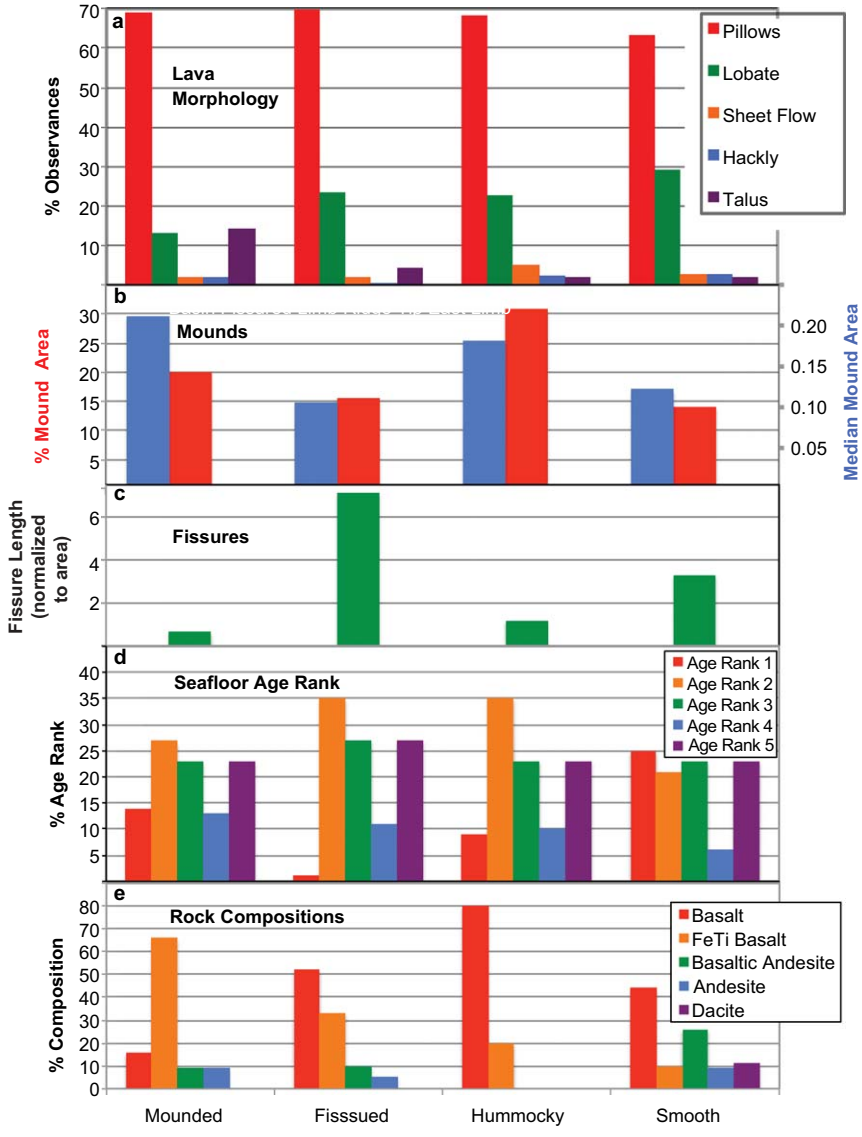

Figure 9. Characteristics of each of the four seafloor terrains (supervised classification; see Figure 8a). (a) Lava morphologies determined from seafloor observations; examples of each morphology are shown labeled in Figures 4 and 6 (terminology after *Perfit* [2001]). (b) Mound characteristics derived from digitized pillow mounds (as shown in Figure 7b); in red, percentage of terrain area covered by mounds; in blue, median mound area (km^2). (c) Normalized fissure length, calculated as total length of fissures (km) determined from digitized traces of fissures (as shown in Figure 7b), divided by terrain area (km^2). (d) Percentages of seafloor photographs with each relative age rank. (e) Percentages of each rock composition type [*Wanless et al.*, 2012].

data (Figure 7b), as described in Supplement 2 of the supporting information. The distribution of geologic features and other characteristics among the terrains is shown in Figure 9.

[28] The "Smooth" terrain is dominantly found along the northern portion of the east limb and extends ~4 km west from the ridge crest by to the edge of the area mapped by sonar (Figure 10a). This terrain is characterized as having the least area covered by mounds and those that are present are relatively small (Figure 9b). It is also the terrain with the greatest percentage of young (RAR 1) seafloor (Figure 9d). The ratio of pillows to lobate flow morphologies (Figure 9a) is lower here than elsewhere in the study area (2:1) although still considerably higher than typical elsewhere along this segment of the EPR [*Kurras et al.*, 2000; *White et al.*, 2002; *Fundis et al.*, 2010].

[29] The "Fissured" terrain is found along the east limb south of 9°04′N and along much of the west

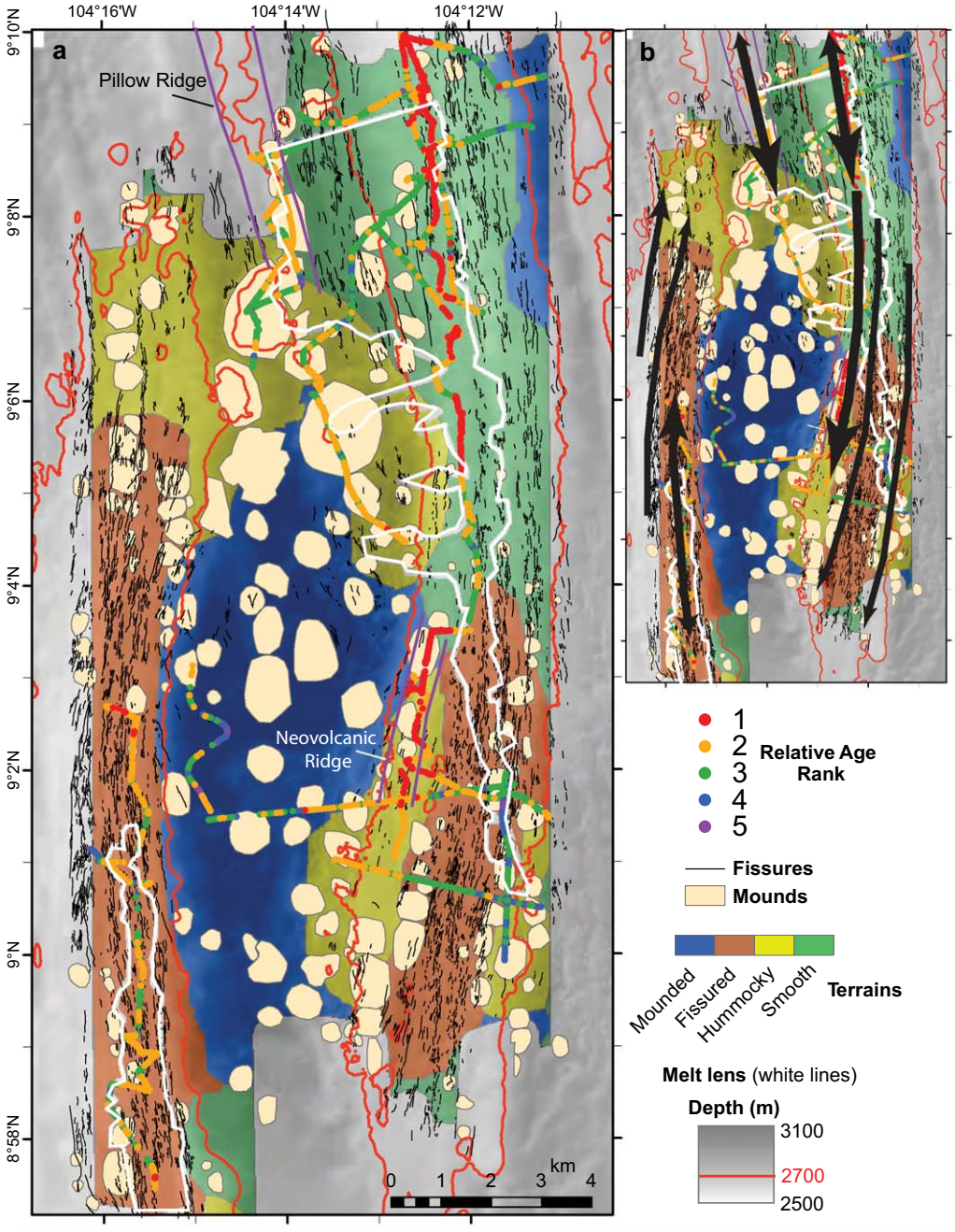

Figure 10. (a) Combined map including fissures (black lines), mounds (rounded beige areas), and seafloor terrains for the supervised classification (colored fields) based on *DSL-120A* backscatter data (Figures 7b and 8a). Also shown are seafloor age ranks (colored dots), bathymetry (gray shading with 2700 m contour highlighted by red lines), and the outline of the melt lens (gray lines) of *Kent et al*. [2000]. The pillow ridge and neovolcanic ridge described in the text are outlined in purple. (b) Schematic illustration of diking events, superimposed on Figure 10a. Recent to older diking events are illustrated by progressively thinner black lines. Directions of dike propagation are indicated by arrowheads, with larger arrowheads indicating the dominant propagation direction.

limb (Figure 10a). As the name suggests, the distinguishing feature within this terrain is the high density of fissures (7 km fissure length/km^2), almost double that of any other terrain (Figure 9c). Pillow mounds are smaller here than in other terrains and cover a relatively small area (Figure 9b). The ratio of pillow to lobate flow morphologies is about 3:1, and talus is more common here than in

the Smooth and Hummocky terrains (Figure 9a), as expected for an area experiencing significant brittle deformation.

[30] The "Hummocky" terrain occurs at the northern tip of the west limb, wrapping around it to the east, and both to the east and west of the Fissured terrain on the east limb near its tip (Figure 10a). In this terrain, pillow mounds cover the greatest area of seafloor, and the pillow mounds are relatively large (Figure 9b). It also has fewer fissures than either the Smooth or Fissured terrains (Figure 9c).

[31] Finally, the "Mounded" terrain corresponds to the area commonly referred to as the overlap basin (Figure 10a). This terrain is characterized by its high relief, relatively steep volcanic pillow ridges flanked by areas of broad flat lava flows. The mounds in this terrain are the most abundant and of largest median area in our study area (Figure 9b). It has the fewest faults and fissures and the greatest percentage of talus (Figures 9a and 9c).

[32] On the scale of the OSC as a whole, our terrain modeling results correlate remarkably well with the spatial distribution and characteristics of the melt sills described by *Kent et al*. [2000] and *Singh et al*. [2006] (Figure 10a). Specifically, the widest and shallowest melt sill is located only beneath the Smooth terrain; and both the melt sill and Smooth terrain extend from the east limb axis to ~4 km west. The Fissured terrains on both limbs overlie narrow, deep and melt-poor sills [*Kent et al*., 2000; *Singh et al*., 2006]. Furthermore, neither the Hummocky nor the Mounded terrains overlie seismically detected melt sills, yet both contain many volcanic mounds combined with few fissures, suggesting abundant volcanic activity over longer timescales. Mounded terrain corresponds well with thicker seismic Layer 2A, and corroborates interpretation of thicker Layer 2A as volcanic in origin [*Bazin et al*., 2001]. Combining these results with information on seafloor age, photo-geology, and lava petrology, and geochemistry allows us to constrain processes of crustal accretion and evolution.

6. Discussion

[33] A primary motivation of our study of the 9N OSC is to explore the relationships between melt distribution at depth and magmatism on the seafloor. An unprecedented body of geophysical work on the OSC documents subsurface magma storage systems that are highly variable in spatial distribution and melt abundances [e.g., *Kent et al*., 2000; *Bazin et al*., 2003; *Singh et al*., 2006; *Dunn et al*., 2001; *Toomey et al*., 2007]. Previous work has led to hypotheses on the pathways that bring melt from depth to the surface—hypotheses that were difficult to test with existing data [*Sempere and Macdonald*, 1986a; *Carbotte and Macdonald*, 1992; *Langmuir et al*., 1986; *Natland et al*., 1986]. Assuming that the characteristics of the melt lens studied in 1997 [e.g., *Kent et al*., 2000] are relevant to seafloor characteristics we observed in 2007, our data allow us to test hypotheses and prevailing assumptions about the links between melt at depth and surface eruptions. Below, we synthesize our findings in the context of previous work in each OSC area, and summarize in section 6.5.

6.1. Northern East Limb and Off-Axis Eruptions

[34] In the northern portion of our study area, photographic results show that the youngest volcanism occurs along the bathymetric east limb axis and that seafloor age generally increases off-axis to the east or west, consistent with seafloor spreading (Figures 3 and 10). The expected increase in seafloor age is interrupted, however, at the pillow ridge, which exhibits consistently younger ages (~RAR 2) than seafloor closer to the axis. These findings suggest that recent volcanism in the northern area occurs in only two places: along the east limb bathymetric axis and on the pillow ridge 4 km to its west, with only sporadic recent volcanism in between. This is also consistent with our terrain modeling results, which show that the Smooth terrain extends west from the axis and transitions to Hummocky terrain in the vicinity of the pillow ridge (Figure 10a), indicating a change in the style of magmatism that includes an increase in the number and size of volcanic mounds. These findings also support the results of detailed bathymetric analysis suggesting that the off-axis pillow ridge is volcanically active [*Tong et al*., 2003; *Combier*, 2005].

[35] Eruption ages determined by U-series isotope studies [*Waters et al*., 2013] support our estimates based on photographic images. Lavas from the northern east limb axis have U-series age limits of <0.1 ka (Figure 3), consistent with recent eruption (RAR 1). ^{230}Th-^{226}Ra model ages from the pillow ridge average 1.0 ka in age, despite the fact that crust at this location should be ~68 ka (assuming

half-spreading rate of 5.5 cm/yr). Only one sample (J265-32) recovered from the basin between the axis and the pillow ridge was dated radiometrically, yielding a model age of 0.7 ka. This sample, recovered from an area of apparently younger off-axis seafloor, may be part of a lava flow originating on-axis or may provide evidence of sporadic off-axis eruptions within the basin. However, the vast majority of photographs within the basin show much older seafloor (Figures 3 and 10) suggesting little recent magmatic activity between the axis and pillow ridge.

[36] Based on available data, it appears that off-axis volcanism in this region is localized over the western edge of the melt sill. One possible explanation for this is that off-axis melt within the sill exploits growth faults associated with abyssal hill formation [*Macdonald et al*., 1996]; in this case, the position of the pillow ridge over the western edge of the sill is largely coincidental. A more intriguing possibility, however, emerges from a recent study of dike intrusion processes at the 9°50′N area of the EPR [*Germanovitch et al*., 2011]. Based on modeling of fracture mechanics, these authors show that dikes are more likely to initiate near the edges—rather than at the center—of an axial magma sill, because tensile stresses are concentrated near the sill margins. This model would explain the origin of the pillow ridge (above the western edge of the melt sill), as well as volcanism on-axis above the eastern margin of the melt sill. The model is also supported by seismic results that show that the roof of the melt sill has two elevated ridges, one beneath the axis and the other beneath the pillow ridge, consistent with an elevation of isotherms associated with diking [*Combier et al*., 2008; *Tong et al*., 2002].

[37] Assuming that the dike intrusion model described above is correct, this offers an opportunity to explore the continuity of the melt sill by comparing the compositions lavas collected on-axis and along the pillow ridge. A common way to identify distinct magma sources relies on the use of radiogenic isotope compositions or incompatible trace element ratios [e.g., *Zindler et al*., 1984]. However, all samples analyzed from the east limb of the 9N OSC have similar, incompatible trace element-depleted characteristics and isotopic compositions [*Wanless et al*., 2010; *Waters*, 2013], and therefore cannot be used to identify distinct mantle sources or melt reservoirs. Nevertheless, other geochemical and petrologic differences between the east limb axial and pillow ridge lavas suggest distinct magmatic histories and melt delivery systems.

[38] With respect to major elements, more than half of the lavas recovered on-axis are andesites and dacites (Figure 9e) that formed through significant extents of fractional crystallization and crustal assimilation [*Wanless et al*., 2010]. In contrast, samples from the pillow ridge are dominantly basaltic (ferrobasalts with ~7.5 wt.% MgO), and exhibit no evidence of crustal assimilation. Based on these findings, *Wanless et al*. [2012] conclude that there is no mixing between axial and pillow ridge magmas, and that the processes that lead to the observed range of evolved magmas (crystallization, assimilation, and mixing of contiguous magma bodies) occurred relatively recently only beneath the east limb axis. This difference in shallow melt storage and evolution is also consistent with seismic evidence suggesting variable distribution of melt within the wide melt sill, with continuous melt-rich areas imaged beneath the axis but discontinuous pockets of melt off-axis [*Kent et al*., 2000; *Singh et al*., 2006].

[39] Support for the idea that unusual magmatic processes occur beneath the east limb comes from the finding of ^{210}Pb excesses in axial ferrobasalts and basaltic andesites [*Waters et al*., 2013]. This signature, while common in arc magmas, is highly unusual in MORB, and appears to require gas-magma fractionation of ^{222}Rn from ^{226}Ra (in the ^{238}U decay series ^{226}Ra-^{222}Rn-^{210}Pb). *Waters et al*. [2013] propose a scenario in which bubbles containing ^{222}Rn stall in the subaxial basalt sill beneath a viscous, dacitic magma cap; ^{210}Pb accumulates by decay and the ^{210}Pb-enriched basalt periodically mixes with the evolved melt and erupt as ferrobasalt. While no ^{210}Pb excesses were found in the ~1 ka-old pillow ridge lavas, this is not surprising because the short half-life of ^{210}Pb (22.6 years) leads to secular equilibrium within ~100 years. Nevertheless, this work, and that of *Wanless et al*. [2010], emphasize the unusual magmatic conditions required to produce the east limb axial lavas, in contrast to those of the pillow ridge.

[40] Petrographic results provide further support for the separate origin of magmas feeding the axis and those feeding the pillow ridge. *Zaino et al*. [2008] found that phenocryst abundances exhibit systematic spatial variations: samples from the northern east limb axis are dominantly aphyric while samples from the pillow ridge (as well as the east limb tip described below) are uniformly more crystal-rich (Figure 11). These spatial differences in phenocryst abundances are not related to differences in magma compositions: east limb axial and pillow ridge basalts have a similar range

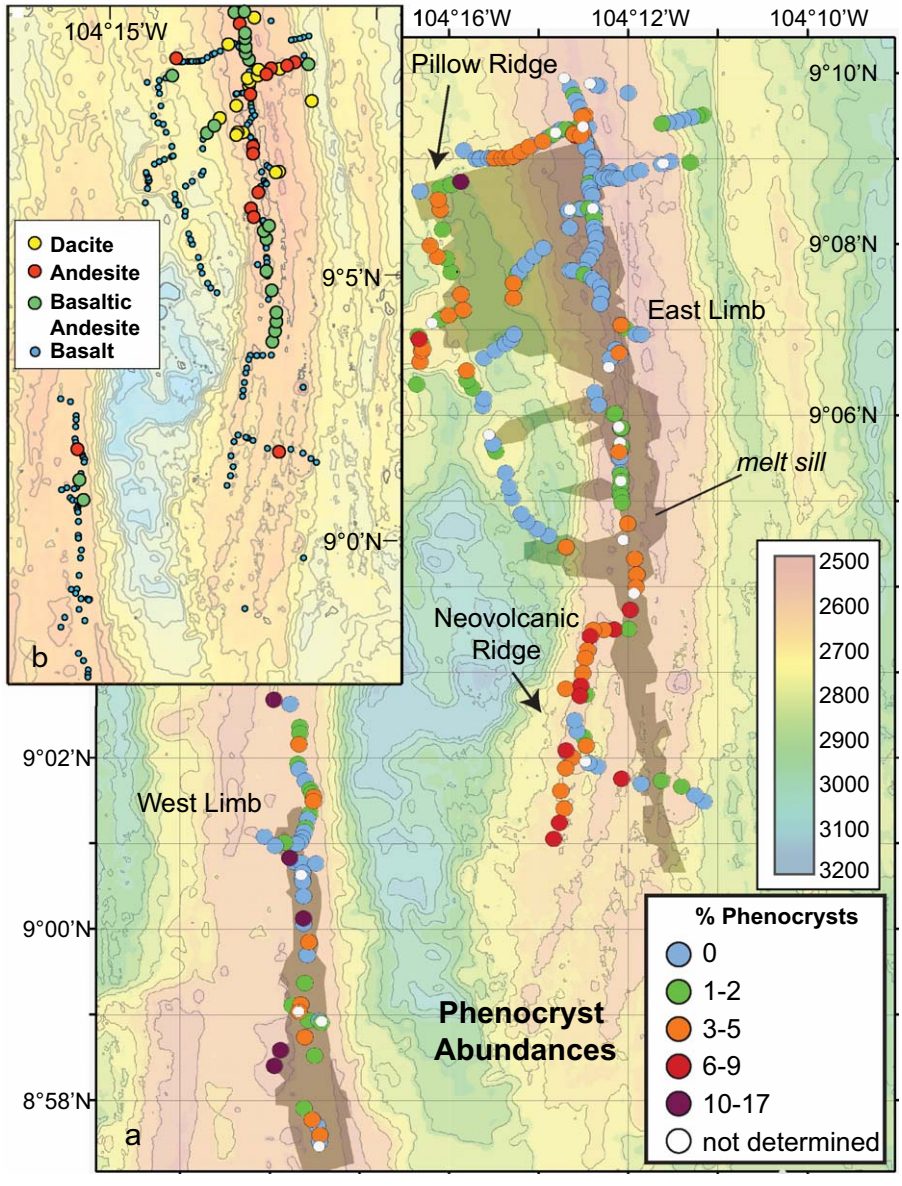

Figure 11. (a) Phenocryst abundances in 9N OSC lavas, color-coded (see legend) for percent by volume [*Zaino et al*., 2008]. On average, higher phenocryst abundances occur in lavas from the south end of the east limb and in lavas from the off-axis pillow ridge; lavas from the northern east limb axis are typically aphyric or sparsely phyric. Lavas from the west limb span a wide range in phenocryst abundances with no spatial systematics. (b) Lava compositions color-coded (see legend) to distinguish dacite (>62 wt.% SiO_2), andesite (57–62 wt.% SiO_2), basaltic andesite (52–57 wt.% SiO_2), and basalt <52 wt.% SiO_2) [modified from *Wanless et al*., 2010].

of MgO contents but differ in their crystal contents (axial andesites and dacites are also aphyric). This suggests that some physical process leads to the occurrence of phenocrysts in the pillow ridge magmas but not in the axial magmas.

[41] One possible explanation for the greater phenocryst abundances in the pillow ridge lavas draws upon the well-documented effects of flow differentiation in igneous dikes [e.g., *Komar*, 1972]. As magma flows within a dike, mechanical interactions between phenocrysts in the melt give rise to grain-dispersive pressure, leading to concentration of phenocrysts in the flowing dike center [e.g., *Brouxel*, 1991; *Ross*, 1986; *Chistyakova and Latypov*, 2009; *Zurevinski and Mitchell*, 2011]. The farther magma (melt + crystals) travels in a

propagating dike, the more crystal-rich the magma may become. The greater phenocryst contents of pillow ridge lavas compared to east limb axial lavas may result from the greater vertical or horizontal distance the magma traveled during dike propagation prior to eruption. Moreover, the fact that none of the pillow ridge phenocrysts are in equilibrium with their host magmas, having crystallized from a more primitive melt, suggests that the phenocrysts were entrained prior to intrusion, and that little if any crystallization occurred during relatively rapid magma migration and eruption [*Zaino et al*., 2008].

6.2. Southern East Limb and Flanks

[42] A significant change in the character of the east limb occurs south of ~9°4′N. Here the Smooth terrain of the northern east limb transitions to Fissured terrain sandwiched by a large expanse of Hummocky terrain to the west and a smaller portion to the east, and the seafloor fabric begins to curve toward the southwest (Figure 10a). Photographic data show that the locus of young volcanism tracks this curvature but cuts more sharply to the southwest, forming a neovolcanic ridge that hugs the edge of the overlap basin (Figures 3 and 10). U-series age constraints indicate that lavas erupted along the neovolcanic ridge are <0.1 ka (Figure 3) [*Waters et al*., 2013]. Despite the curvature of both the seafloor fabric and neovolcanic ridge, the plunging melt sill beneath the east limb continues along the same trend exhibited farther north, cutting across the seafloor fabric.

[43] The spatial divergence of the neovolcanic zone and the plunging melt sill has been attributed to a decoupling of the stress field of the brittle upper crust from that of the ductile lower crust and upper mantle [*Combier et al*., 2008]. In this model, the curvature of seafloor features results from shallow crustal stresses associated with the interaction of the east and west limbs of the OSC [*Pollard and Aydin*, 1984; *Sempere and Macdonald*, 1986b], while the regional stress field associated with plate spreading controls the ductile lower crust and upper mantle, causing melt at depth to align closer to perpendicular to spreading direction [cf., *Toomey et al*., 2007].

[44] Our photographic data show that this decoupling of shallow and deep stress fields manifests itself in a decoupling between surface volcanism and underlying melt bodies. Only old seafloor overlies the plunging melt sill, suggesting that the sill is the source of little if any recent magmatism in this area (Figures 3 and 10). Conversely, no melt body has been imaged beneath the southern neovolcanic ridge, suggesting that the magma that feeds this ridge is derived from elsewhere.

[45] These findings support previous work [*Tong et al*., 2002; *Combier et al*., 2008; *White et al*., 2009] suggesting that the neovolcanic ridge forms by southward dike propagation, tapping melt from the magma-rich axial melt lens 6–10 km to the north. Additional support for this view comes from geochemical and petrologic results. First, like the axial lavas analyzed further north, basalts from the neovolcanic ridge have ^{210}Pb excesses (Figure 3) [*Waters et al*., 2013]. But in contrast to the northern axis, where lavas range from basalt to dacite, only basalts erupt along the neovolcanic ridge. Therefore, the conditions that appear necessary to produce ^{210}Pb excesses in the north (a viscous dacite cap that causes the underlying basalt melt to accumulate ^{222}Rn-bearing bubbles) do not exist along the neovolcanic ridge. This suggests that the neovolcanic ridge derives its magma from the axial melt lens to the north where the isotopic disequilibrium is produced. A second line of evidence supporting southward dike propagation is our finding that lavas from the neovolcanic ridge, like those from the off-axis pillow ridge, are significantly more phyric than east limb axial lavas to the north (Figure 11), and phenocrysts are not in equilibrium with their host magma. As argued above with respect to the pillow ridge, the phyric nature of these lavas may result from flow differentiation during dike propagation [*Brouxel*, 1991; *Komar*, 1972], suggesting southward transport of magma from the northern east limb axis.

[46] Based on detailed bathymetric analysis, *Combier* [2005] suggested that the southern east limb consists of a series of curved volcanic ridges formed by southward dike propagation. Our terrain modeling results, which show a symmetrical pattern of Fissured terrain sandwiched by two areas of Hummocky terrains (Figure 10a), are consistent with this view and suggests the following scenario. Repeated southward diking events, like those that formed the neovolcanic ridge (situated within Hummocky terrain), build the series of curved volcanic ridges that as a whole comprise both the Fissured and Hummocky terrains. Periodic episodes of extension, perhaps due to noneruptive dike intrusion, lead to fissuring within a central band, producing the distinctive Fissured terrain. The observation that volcanic mounds, which appear to be associated with the curved volcanic ridges, are in some cases cut by fissures while in other cases

appear to overprint fissures (Figure 7) suggests that episodes of eruption and extension occur synchronously or alternate with one another over short time scales.

[47] With the caveat that our photographic coverage is limited, we can nevertheless place some constraints on the timing and relative sequence of volcanic events along the southern east limb. We know from photographic and radiometric data that the neovolcanic ridge is young, ~100 years old (RAR = 1) (Figure 3) [*Waters et al*., 2013]. Moving east along a traverse from the neovolcanic ridge, across the Fissured terrain, seafloor shows a regular progression in relative age rank to RARs 3–5 (Figure 10a). To the extent that our calibration of the relative age rank provides a rough estimate of the age of seafloor older than RAR 2 (see Supplement 1 in the supporting information), this suggests that seafloor at the eastern limit of our survey is >36 ka. These findings suggest further that over the past few tens of thousands of years, southward diking has repeatedly cut sharply toward the inside curve (west) of the previous volcanic ridge. Interestingly, seafloor ages also increase moving southward within the region (compare, e.g., the two traverses within the Fissured terrain in Figure 10a), suggesting that periodic diking events in the past extended further south than the most recent event at the neovolcanic ridge.

6.3. The West Limb

[48] The west limb is composed dominantly of Fissured terrain, capped at its northern tip by Hummocky terrain that spreads eastward and merges with the southern extension of the pillow ridge (Figure 10a). The transition from Fissured to Hummocky terrain coincides with the appearance of well-defined volcanic ridges [*Combier*, 2005], where previous photographic results [*Sempere and Macdonald*, 1986a] identified a mixture of young and old seafloor. Our limited photographic survey shows that, in contrast to ubiquitous young seafloor along the east limb, the west limb axis exhibits a mixture of medium-aged seafloor (RAR 2 and 3), consistent with previous studies suggesting less magmatic activity [e.g., *Combier*, 2005]. Notably, however, an isolated area of young seafloor (RAR 1) was identified a few kilometers north of the melt sill (Figure 3), raising the possibility of sporadic northward diking events emanating from the sill to the west limb tip, reminiscent of the diking events postulated for the southern east limb (section 6.2). Interestingly, like samples from the southern east limb, west limb lavas tend to be phyric (up to 17%) (Figure 11) [*Zaino et al*., 2008], possibly due to lower magma supply relative to cooling rates and/or flow differentiation during dike propagation.

[49] Overall, our results suggest that the west limb experiences infrequent diking events, producing the observed mixture of young and old seafloor. These diking events likely propagate northward, suggested by the young seafloor north of the melt sill; in the past, intrusion and eruption may have extended as far as the Hummocky terrain at the northern west limb tip, producing the northern volcanic ridges. Magmatism appears to be synchronous with and overprinted by episodes of amagmatic extension and fissuring, perhaps due to dike intrusions at depth, producing the Fissured terrain that dominates the west limb axis. Further study of the northern end of the west limb is needed to determine how far recent eruptions extend on this "dying" limb.

6.4. The Overlap Basin (Overlap Region)

[50] Despite decades of study of overlapping spreading centers, the processes that lead to the formation of overlap basins remain elusive. The issue is complicated, in part, by one of definition, with recent studies using the term overlap basin to describe a broad region between the overlapping limbs, which likely includes seafloor produced in different ways. Terrain modeling is particularly useful in this regard because it objectively identifies differences in seafloor characteristics, thus isolating the effects of distinct magmatic and tectonic processes.

[51] The overlap region at the 9N OSC is dominated by a deep central zone of Mounded terrain, which along its margins abuts each of the three other terrains (Figures 8 and 10). Of particular, interest are the two areas of Hummocky terrain along the basin's eastern margin, that despite their greater depth, share the same terrain characteristics of the shallower adjacent east limb (Figure 10a). This provides independent support for previous work [e.g., *Bazin et al*., 2001; *Tong et al*., 2003, 2005] suggesting that particularly the southeastern portion of the overlap region shares a close genetic relationship with the propagating east limb.

[52] Our photographic results within the overlap region further support the distinction between Mounded and Hummocky terrains (Figure 10a). Seafloor within the imaged areas of Hummocky terrain is relatively young (RAR 2), while that

within the Mounded terrain shows a mixture of young to old seafloor (RAR 2–5). The latter is consistent with the view that the deepest part of the basin (the Mounded terrain) experiences sporadic eruptions that lead to the development of large volcanic mounds [*Bazin et al*., 2001; *White et al*., 2009]. *White et al*. [2009] hypothesize that these volcanic mounds tap small ephemeral melt bodies, possibly originating in the upper mantle low-velocity zone that spans the basin [*Dunn et al*., 2001; *Toomey et al*., 2007].

6.5. Recent Evolution of the OSC

[53] Our current observations of processes occurring at the 9N OSC represent a snapshot in time in the long-term evolution of this discontinuity. In a seminal study of the kinematics of the OSC, *Carbotte and Macdonald* [1992] showed that over the past 1.8 Ma the OSC has migrated southward episodically at an average rate of 42 mm/yr, leaving an off-axis V-shaped wake of abandoned ridge tips, overlap basins, and disrupted seafloor. Rift tip abandonment occurred either by decapitation, during which the *en echelon* limbs link and a relict overlap basin is rafted off-axis, or by self-decapitation in which a splay of one limb curves sharply inward toward the overlap basin, cutting off its former ridge tip [*Macdonald et al*., 1988].

[54] During the past decade, studies of the OSC have provided a more detailed understanding of the recent kinematics of accretion, particularly along the propagating east limb. Based on bathymetry and melt sill characteristics, *Tong et al*. [2002] proposed that the features we call the pillow ridge and the southern neovolcanic ridge represent incipient stages in the self-decapitation of the propagating east limb. *Combier et al*. [2008] and *White et al*. [2009] suggested further that these features develop by lateral southward dike propagation. By constraining seafloor age (through photography and U-series age dating) [*Waters et al*., 2013] and seafloor characteristics (through terrain modeling), the results we report here both support this view and provide additional information on accretion at the OSC.

[55] A conceptual illustration of our preferred interpretation is presented in Figure 10b. Overall, our results suggest that along the northern east limb axis, eruptions occur in a relatively narrow band over the eastern edge of the wide melt sill. Moving south along the east limb axis, in the vicinity of 9°04–05′N, the limb begins to curve in response to the rotation of the stress field [e.g., *Pollard and Aydin*, 1984]; here, accretion occurs

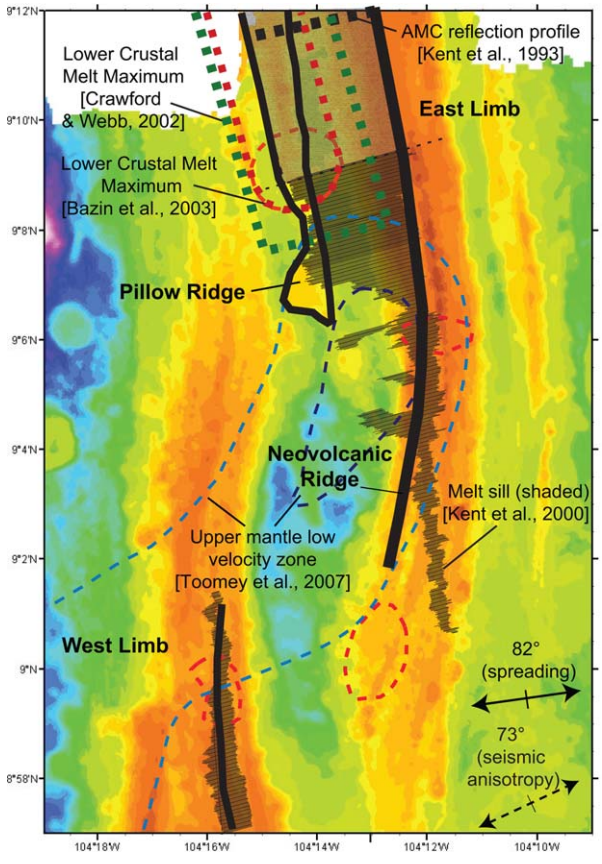

Figure 12. Published geophysical data superimposed on bathymetry and tectonic interpretation. East limb and west limb neovolcanic zones (curved black lines), pillow ridge (black outline). Data from the ARAD seismic tomography experiment: melt sill (shaded gray) [*Kent et al*., 2000], low-velocity anomaly maxima at 2.3 km bsf interpreted as melt (red dashed lines) [*Bazin et al*., 2003]. Lower crustal melt maxium based on compliance measurements (green dashed lines) [*Crawford and Webb*, 2002], axial magma chamber seismic reflection profile (thick dashed black line) [*Kent et al*., 1993], upper mantle low velocity zones at 9 km bsf (dashed blue lines; darkest blue indicates lowest *P* wave velocity) [*Toomey et al*., 2007]. The northern extent of the ARAD study is indicated by thin black dotted line; extensions of the melt sill, lower crust seismic anomaly and compliance data to the north of this line represent our interpretation. Spreading direction (82°) shown as black line with arrows [*Gripp and Gordon*, 2002] and direction perpendicular to interpretation of mantle seismic anisotropy [*Toomey et al*., 2007] shown as dashed line with arrows.

by southward diking that cuts sharply toward the overlap basin and taps magma from the melt sill >6 km to the north, producing the neovolcanic ridge. Evidence for previous southward diking events can be seen in the progressively older volcanic ridges that fan out to the east and south of the current neovolcanic ridge, suggesting that each new intrusion typically is emplaced west of the

prior intrusion. The fact that the current neovolcanic ridge does not appear to extend as far south as older volcanic ridges suggests that overall southward OSC migration occurs through periodic southward jumps (upper crustal intrusions) of differing lengths.

[56] In the northern portion of our study area, photographic coverage suggests that the dominant site of off-axis eruptions occurs along the pillow ridge, which overlies the western edge of the wide melt sill. The simplest explanation for the formation of the pillow ridge is that it taps melt vertically from the sill beneath it [*Combier et al*., 2008]. However, as explored below, a number of lines of evidence suggest that a component of horizontal, southward dike propagation may also play a role in its formation.

[57] The relative importance of vertical versus horizontal magma transport during subaxial diking events has been the subject of much debate [e.g., *Bergmanis et al*., 2007; *White et al*., 2002; *Stewart et al*., 2002, 2003; *Marjanović*, 2013]. *Carbotte et al*. [2013] argue that in areas of the EPR where abundant melt is present, the predominant mode of transport may be vertical, while near large axial discontinuities, lateral transport may play a greater role. Indeed, among the many factors that govern the migration of dikes at spreading centers [e.g., *Rubin*, 1995], modeling suggests that dikes will tend to propagate toward ridge segment ends as a result of the thickening of the elastic-brittle lithosphere [*Grandin et al*., 2012]. This argues in favor of a component of southward dike propagation toward the 9N OSC.

[58] Furthermore, real-time studies of subaerial dike intrusion events suggest that dikes may travel tens of kilometers horizontally, although the extent to which propagation of seismicity reflects magma transport is debated [e.g., *Einarsson and Brandsdottir*, 1980; *Bjornsson*, 1985; *Dziak et al*., 2007; *Keir et al*., 2009; *Wright et al*., 2006]. Such studies often describe the formation of fissure-erupted volcanic ridges, such as those associated with Kilauea and Mauna Loa in Hawaii or Laki and Krafla in Iceland, which are believed to have formed through lateral dike propagation [e.g., *Björnsson et al*., 1977; *Decker*, 1987; *Thordarson and Self*, 1993; *Thordarson and Larsen*, 2007]. We speculate that a similar process at the 9N OSC may have led to the formation of the pillow ridge, which becomes a more prominent feature in terms of elevation and relief north of our study area (Figure 12).

[59] With respect to the west limb, while our limited photographic traverse over the narrow melt sill shows a mixture of relatively young and older seafloor with no spatial systematics, tantalizingly, recent eruptions were found ~3 km north of the sill (Figure 5). In the absence of additional information on seafloor age, we speculate that west limb currently experiences intermittent northward diking events that extend a few kilometers north of the sill, and tap melt from more robust portions of the sill to the south (Figure 10b). Further investigation of the northern end of the west limb is needed to better understand the timing of events involved in this limb's retreat.

6.6. OSC Migration

[60] Results presented here combined with previous findings have advanced our understanding of the kinematic evolution of the 9N OSC. But our understanding of the factors that drive the southward migration of the OSC remains elusive. Various hypotheses have been advanced to explain the direction of OSC migration. In one class of models, propagation of the advancing limb results from tectonic factors, such as excess along-axis topographic relief [e.g., *Phipps-Morgan and Parmentier*, 1985], differential stress between the lithospheric plates [*Lonsdale*, 1994], or the relative lengths of adjacent ridge segments [*Macdonald et al*., 1991]. Alternative models attribute advance of the propagating limb to episodic pulses of magma, possibly resulting from large-scale focusing of mantle upwelling at segment centers and along-axis melt migration toward magma-starved segment ends such as OSCs [e.g., *Macdonald et al*., 1988].

[61] The finding of abundant crustal melt at the 9N OSC [e.g., *Kent et al*., 2000; *Crawford and Webb*, 2002; *Bazin et al*., 2003; *Singh et al*., 2006] and normal, albeit relatively evolved, magma geochemistry [*Wanless et al*., 2012] argues against the idea that this discontinuity experiences reduced magma supply and migrates in response to along-axis pulses of magma from a robust segment center. Nevertheless, the presence of abundant crustal melt, particularly associated with the propagating east limb, encourages the view that more *local* magma supply leads to propagation of the east limb and the overall southward migration of the OSC. Within the OSC region, existing geophysical data (Figure 12) suggest the following general scenario for migration of melt from the upper mantle to the east limb region. In the upper mantle (~9 km below seafloor) a broad swath of low seismic

velocities, interpreted as partial melt, cuts diagonally SW-NE across the OSC [*Dunn et al*., 2001; *Toomey et al*., 2007]. This melt percolates into the lower crust, apparently preferentially in the region north of the overlap basin between the west limb tip and east limb [*Crawford and Webb*, 2002; *Bazin et al*., 2003]. Lower crustal melt in this region rises and pools, spreading eastward along the base of a permeability barrier, possibly the sheeted dike complex, creating the wide off-axis melt sill [*Kent et al*., 2000]. Diking events initiate near the margins of the sill and transport magma to the surface, both vertically and horizontally, but with net southward dike propagation over time, leading to the overall southward migration of the OSC.

[62] Based on what is currently known, we support this scenario, but note that it raises some puzzling issues. The first concerns the poor spatial correlation between melt imaged in the upper mantle and that in the crust (Figure 12). As noted by *Bazin et al*. [2003], the misalignment between the melt-rich region of the lower crust and that of the upper mantle would require a complex trajectory of melt migration from depth. While it is possible that in the past the relative positions of upper mantle and crustal melt were vertically aligned, recent geophysical work suggests an alternate explanation. A magnetotelluric study of melt distribution in the mantle at 9°30′N on the EPR [*Key et al*., 2013] showed that while mantle shallower than about 20 km has generally high resistivity (interpreted as low porosity and low melt), an isolated higher melt channel extends from the EPR axis eastward about 10 km; this suggests efficient transport of magma within the upper mantle ~10 km toward the axis. This higher porosity channel coincides with an area where seismic tomography identified an off-axis, low velocity anomaly in the upper mantle, like that imaged beneath the 9N OSC [*Toomey et al*., 2007]. To the extent that these findings are relevant to conditions at the 9N OSC, they indicate that melt imaged in the upper mantle may travel significant horizontal distances as it migrates from the upper mantle to the crust.

[63] This raises a second perplexing question: why is melt from the upper mantle preferentially focused toward the north rather than toward the south of the OSC basin? In other words, why does supply of magma favor the east limb, leading to its southward migration over most of the past ~2 Ma [*Carbotte and Macdonald*, 1992]? We speculate that there may be a reinforcing feedback mechanism, such that higher porosity pathways in the lower crust, once established, continue to be preferentially exploited. Previous seismic [*Kent et al*., 1993] and seafloor compliance [*Crawford and Webb*, 2002] studies show that the wide asymmetric melt sill at the OSC persists north of the OSC (Figure 12). *Kent et al*. [1993] speculated that just as the wide melt sill at the OSC extends west from the east limb to the tip of the dying limb, the westward displacement of the melt lens north of the OSC may approximate the previous location of the west limb as it recedes southward. Building on this idea, but emphasizing the plumbing systems beneath the sill, we suggest that the thermal and porosity structure established in the lower crust at the OSC may persist long after the surficial tectonic features of the OSC have migrated southward.

7. Conclusions

[64] Integration of our terrain modeling and photogeologic results with existing geophysical and geochemical data at the 9N OSC provides a rich perspective on the linkages between eruptive activity and the distribution of melt at depth. Modeling of seafloor texture identified four distinct terrains, suggesting that diverse tectonic, magmatic, hydrothermal, and sedimentary processes produce seafloor textures that can be described in a small number of dominant modes. Our finding that the classic tectonic divisions commonly used to describe OSCs (ridge axes, ridge tips, overlap basin) often consist of multiple terrains highlights the range of processes that occur in each tectonically defined region, and encourages a more nuanced perspective on OSC development and evolution.

[65] Our results show that recent eruptions above the 4 km wide asymmetric melt sill beneath the east limb occur dominantly along the sill's east and west margins, erupting respectively along the east limb axis and the anomalously young off-axis pillow ridge. The only recent volcanism observed along the southern east limb forms a neovolcanic ridge that curves westward into the overlap basin, sharply diverging from the seismically imaged plunging melt sill. Above the plunging melt sill, only older seafloor is observed, suggesting that this melt body is the source of little if any recent magmatism.

[66] We postulate that both the southern neovolcanic ridge and the pillow ridge form by diking events with a net southward direction of

propagation, leading to the overall southward migration of the OSC. Along the dying west limb, intermittent northward diking events likely occur, but with time dikes extend less far to the north. The wealth of data collected from this region highlights that, at least at ridge axis discontinuities, melt migration from depth to eruption on the seafloor likely involves significant lateral as well as vertical transport.

Acknowledgments

[67] We thank the captain and crew of the R/V Atlantis, the Woods Hole Deep Submergence Laboratory, and the Hawaii Mapping Research Group for enabling a successful cruise. We are grateful to S. Carbotte, T. Becker, and an anonymous reviewer for their thorough reviews, and to G. Kent, S. Carbotte, J. Karson, S. Webb, and Y. Zha for fruitful discussions. J. Jensen provided helpful advice and support on the classification methods. We note with sadness the passing of Karen Von Damm, our dear friend, colleague, and co-investigator in this work. The National Science Foundation and the RIDGE2000 program supported this work through grants OCE0526120 to E.M.K., OCE0525872 to S.M.W., OCE0527075 to M.R.P., and OCE 052705300 to K.W.W.S.

References

Ball, G. H., and D. J. Hall (1965), ISODATA, a novel method of data analysis and pattern classification, Tech. Rep. AD 699616, Stanford Res. Inst., Menlo Park, Calif.

Ballard, R. D., J. Francheteau, T. Juteau, C. Rangan, and W. Normark (1981), East Pacific rise at 21°N: The volcanic, tectonic, and hydrothermal processes of the central axis, *Earth Planet. Sci. Lett.*, *55*, 1–10, doi:10.1016/0012-821x(81)90081-9.

Baran, J. M., J. R. Cochran, S. M. Carbotte, and M. R. Nedimović (2005), Variations in upper crustal structure due to variable mantle temperature along the Southeast Indian Ridge, *Geochem. Geophys. Geosyst.*, *6*, Q11002, doi:10.1029/2005GC000943.

Bazin, S., et al. (2001), Three-dimensional shallow crustal emplacement at the 9°03′N overlapping spreading center on the East Pacific Rise: Correlations between magnetization and tomographic images, *J. Geophys. Res.*, *106*, 16,101–16,117, doi: 10.1029/2001JB000371.

Bazin, S., et al. (2003), A three-dimensional study of a crustal low velocity region beneath the 9°03′N overlapping spreading center, *Geophys. Res. Lett.*, *30*(2), 1039, doi:10.1029/2002GL015137.

Bergmanis, E. C., J. Sinton, and K. H. Rubin (2007), Recent eruptive history and magma reservoir dynamics on the southern East Pacific Rise at 17°30′S, *Geochem. Geophys. Geosyst.*, *8*, Q12O06, doi:10.1029/2007GC001742.

Björnsson, A., K. Saemundsson, P. Einarsson, E. Tryggvason, and K. Grönvold (1977), Current rifting episode in north Iceland, *Nature*, *266*, 318–323, doi:10.1038/266318a0.

Björnsson, A (1985), Dynamics of crustal rifting in NE Iceland, *J. Geophys. Res.*, *90*, B12, 10151–10162

Brouxel, M. (1991), Geochemical consequences of flow differentiation in a multiple injection dike (Trinity ophiolite, N. California), *Lithos*, *26*, 245–252, doi:10.1016/0024-4937(91)90031-F.

Carbotte, S., and K. Macdonald (1992), East Pacific Rise 8°–10°30'N: Evolution of ridge segments and discontinuities from SeaMARC II and three-dimensional magnetic studies, *J. Geophys. Res.*, *97*, 6959–6982, doi:10.1029/91JB03065.

Carbotte, S. M., R. S. Detrick, A. Harding, J. P. Canales, J. Babcock, G. Kent, E. Van Ark, M. Nedimovic, and J. Diebold (2006), Rift topography linked to magmatism at the intermediate spreading Juan de Fuca Ridge, *Geology*, *34*, 209–212, doi:10.1130/g21969.1.

Carbotte, S. M., M. Marjanović, H. Carton, J. C. Mutter, J. P. Canales, M. R. Nedimović, S. Han, and M. R. Perfit (2013), Fine-scale segmentation of the crustal magma reservoir beneath the East Pacific Rise, *Nat. Geosci.*, *6*, 866–870, doi:10.1038/NGEO1933.

Chistyakova, S., and R. Latypov (2009), On the development of internal chemical zonation in small mafic dykes, *Geol. Mag.*, *147*(1), 1–12. doi: 10.1017/S0016756809990343.

Combier, V. (2005), Upper crustal dynamics of the 9°03'N OSC at the East Pacific Rise: Linking surficial and melt sill structures, *Lithos*, *7*, 73–82.

Combier, V., S. C. Singh, M. Cannat, and J. Escartin (2008), Mechanical decoupling and thermal structure at the East Pacific Rise axis 9°N: Constraints from axial magma chamber geometry and seafloor structures, *Earth Planet. Sci. Lett.*, *272*, 19–28, doi:10.1016/j.epsl.2008.03.046.

Crawford, W. C., and S. C. Webb (2002), Variations in the distribution of magma in the lower crust and at the Moho beneath the East Pacific Rise at 9–10 N, *Earth Planet. Sci. Lett.*, *203*, 117–130, doi:10.1016/S0012-821X(02)00831-2.

Decker, R. W. (1987), Dynamics of Hawaiian volcanoes: An overview, *U.S. Geol. Surv. Prof. Pap.*, *1350*, 997–1018.

Detrick, R., P. Buhl, E. Vera, J. Mutter, J. Orcutt, J. Madsen, and T. Brocher (1987), Multi-channel seismic imaging of a crustal magma chamber along the East Pacific Rise, *Nature*, *326*, 35–41, doi:10.1038/326035a0.

Detrick R, J. Sinton, G. Ito, J. Canales, M. Behn, T. Blacic, B. Cushman, J. Dixon, D. W. Graham, and J. Mahoney (2002), Correlated geophysical, geochemical, and volcanological manifestations of plume-ridge interaction along the Galápagos Spreading Center, *Geochem. Geophys. Geosyst.*, *3*, 1–14, doi: 10.1029/2002GC000350.

Dunn, R. A., D. R. Toomey, R. S. Detrick, and W. S. D. Wilcock (2001), Continuous mantle melt supply beneath an overlapping spreading center on the East Pacific Rise, *Science*, *291*, 1955–1958, doi:10.1126/science.1057683.

Dziak, R. P., D. R. Bohnenstiehl, J. P. Cowen, E. T. Baker, K. H. Rubin, J. H. Haxel, and M. J. Fowler (2007), Rapid dike emplacement leads to eruptions and hydrothermal plume release during seafloor spreading events, *Geology*, *35*, 579, doi:10.1130/G23476A.1.

Einarsson, P., and B. Brandsdottir (1980), Seismological evidence for lateral magma intrusion during the July 1978 deflation of the Krafla Volcano in NE Iceland, *J. Geophys.*, *47*, 160–165, doi:10.2172/890964.

Embley, R. W., and W. W. Chadwick Jr. (1994), Volcanic and hydrothermal processes associated with a recent phase of seafloor spreading at the northern Cleft segment: Juan de Fuca Ridge, *J. Geophys. Res.*, *99*, 4741–4760, doi:10.1029/93JB02038.

Escartin, J., S. A. Soule, D. J. Fornari, M. A. Tivey, H. Schouten, and M. R. Perfit (2007), Interplay between faults and lava flows in construction of the upper oceanic crust: The East Pacific Rise crest 9°25'-9°58'N, *Geochem. Geophys. Geosyst.*, *8*, Q06005, doi:10.1029/2006GC001399.

Fornari, D. J. (2003), A new deep-sea towed digital camera and multi-rock coring system, *Eos Trans. AGU*, *84*, 69, doi:10.1029/2003EO080001.

Fundis, A. T., S. A. Soule, D. J. Fornari, and M. R. Perfit (2010), Paving the seafloor: Volcanic emplacement processes during the 2005–2006 eruptions at the fast spreading East Pacific Rise, 9°50′N, *Geochem. Geophys. Geosyst.*, *11*, Q08024, doi:10.1029/2010GC003058.

Germanovich, L. N., R. P. Lowell, and P. Ramondenc (2011), Magmatic origin of hydrothermal response to earthquake swarms: Constraints from heat flow and geochemical data, *J. Geophys. Res.*, *116*, B05103, doi:10.1029/2009JB006588.

Grandin, R., A. Socquet, C. Doubre, E. Jacques, and G. C. P. King (2012), Elastic thickness control of lateral dyke intrusion at mid-ocean ridges, *Earth Planet. Sci. Lett.*, *319–320*, 83–95, doi:10.1016/j.epsl.2011.12.011.

Gripp, A. E., and R. G. Gordan (2002), Young tracks of hotspots and current plate velocities, *Geophys. J. Int.*, *150*, 321–361.

Haralick, R. M., K. Shanmugam, and I. Dinstein (1973), Textural features for image classification, *IEEE Trans. Syst. Man Cybern.*, *SMC3*(6), 610–621.

Harding, A. J., G. M. Kent, and J. A. Orcutt (1993), A multichannel seismic investigation of upper crustal structure at 9 N on the East Pacific Rise: Implications for crustal accretion, *J. Geophys. Res.*, *98*, 13,925–13,913−13,944, doi:10.1029/93JB00886.

Hartley, M. E., and T. Thordarson (2013), The 1874–76 volcano-tectonic episode at Askja, north Iceland: Lateral flow revisited, *Geochem. Geophys. Geosyst.*, *14*, 2286–2309, doi:10.1002/ggge.20151.

Haymon, R. M., D. J. Fornari, K. Von Damm, M. Lilley, M. Perfit, J. Edmond, W. Shanks III, R. Lutz, J. Grebmeier, and S. Carbotte (1993), Volcanic eruption of the mid-ocean ridge along the East Pacific Rise crest at 9°45–52′N: Direct submersible observations of seafloor phenomena associated with an eruption event in April, 1991, *Earth Planet. Sci. Lett.*, *119*, 85–101.

Jensen, J. R. (2005), *Introductory Digital Image Processing: A Remote Sensing Perspective*, vol. *xv*, 3rd ed., 526 pp., Prentice Hall, Upper Saddle River, N. J.

Karson, J. A. (2002), Geologic structure of the uppermost oceanic crust created at fast-to-intermediate-rate spreading centers, *Ann. Rev. Earth Planet. Sci.*, *30*, 347–347, doi:10.1146/annurev.earth.30.091201.141132.

Keir, D., et al. (2009), Evidence for focused magmatic accretion at segment centers from lateral dike injections captured beneath the Red Sea rift in Afar, *Geology*, *37*, 59–62, doi:10.1130/G25147A.1.

Kent, G., A. J. Harding, and J. Orcutt (1993), Distribution of magma beneath the East Pacific Rise between the Clipperton transform and the 9°17′N Deval from forward modeling of common depth point data, *J. Geophys. Res.*, *98*, 13,945–13,969.

Kent, G., A. J. Harding, M. C. Sinha, J. A. Orcutt, P. J. Barton, R. S. White, S. Bazin, R. W. Hobbs, C. H. Tong, and J. W. Pye (2000), Evidence from three-dimensional seismic reflectivity images for enhanced melt supply beneath mid-ocean-ridge discontinuities, *Nature*, *406*, 614–618, doi:10.1038/35020543.

Key, K., S. Constable, L. Liu, and A. Pommier (2013), Electrical image of passive mantle upwelling beneath the northern East Pacific Rise, *Nature*, *495*, 499–502, doi:10.1038/nature11932.

Klein, E., et al. (2007), Medusa Expedition AT15–17 cruise report, 130 pp. doi:10.1594/IEDA/900001.

Komar, D. (1972), Flow differentiation in igneous dikes and sills: Profiles of velocity and phenocryst concentration, *Geol. Soc. Am. Bull.*, *83*, 3443–3448.

Kurras, G. J., D. J. Fornari, M. H. Edwards, M. R. Perfit, and M. C. Smith (2000), Volcanic morphology of the East Pacific Rise crest 9°49′–52′: Implications for volcanic emplacement processes at fast-spreading mid-ocean ridges, *Mar. Geophys. Res.*, *21*, 23–41, doi:10.1023/A:1004792202764.

Langmuir, C. H., J. F. Bender, and R. Batiza (1986), Petrological segmentation of the East Pacific Rise, 5°30′–14°30′N, *Nature*, *322*, 422–429.

Lonsdale, P. (1989), The rise flank trails left by migrating offsets of the equatorial East Pacific Rise axis, *J. Geophys. Res.*, *94*, 713–743, doi:10.1029/JB094iB01p00713.

Lonsdale, P. (1994), Geomorphology and structural segmentation of the crest of the southern (Pacific-Antarctic) East Pacific Rise, *J. Geophys. Res.*, *99*, 4683–4702, doi:10.1029/93JB02756.

Macdonald, K. C., and P. J. Fox (1983), Overlapping spreading centres: New accretion geometry on the East Pacific Rise, *Nature*, *302*, 55–58, doi:10.1038/302055a0.

Macdonald, K. C., P. J. Fox, L. J. Perram, M. F. Eisen, R. M. Haymon, S. P. Miller, S. M. Carbotte, M.-H. Cormier, and A. N. Shor (1988), A new view of the mid-ocean ridge from the behaviour of ridge-axis discontinuities, *Nature*, *335*, 217–225.

Macdonald, K. C., D. S. Scheirer, and S. M. Carbotte (1991), Mid-ocean ridges: Discontinuities, segments and giant cracks, *Science*, *253*, 986–994. doi:10.1126/science.253.5023.986.

Macdonald, K. C., P. Fox, R. T. Alexander, R. Pockalny, and P. Gente (1996), Volcanic growth faults and the origin of Pacific abyssal hills, *Nature*, *380*, 125–129.

Marjanović, M. (2013), Signatures of present and past melt distribution at fast and intermediate spreading centers, PhD dissertation, Columbia Univ. Press, New York.

Natland, J. H., C. H. Langmuir, J. F. Bender, R. Batiza, and C. Hopson (1986), Petrologic systematics in the vicinity of the 9°N non-transform offset, East Pacific Rise, *Eos Trans. AGU*, *67*, 1254.

O'Brien, J. F., and S. M. White, (2007) Deep-tow investigation of crustal magnetization at the 9N overlapping spreading centers on the East Pacific Rise, *EOS Trans. AGU*, *88*(52) Fall Meeting Suppl. Abstract T33B-1349.

Perfit, M. R. (2001), Mid-ocean ridge geochemistry and petrology, in *Encyclopedia of Ocean Sciences*, vol. *3*, edited by J. Steel, S. Thorpe, and K. Turekian, pp. 1778–1788, Academic, San Diego, CA, doi:10.1006/rwos.2001.0096.

Perfit, M. R., and W. W. Chadwick Jr. (1998), Magmatism at mid-ocean ridges: Constraints from volcanological and geochemical investigations, in *Faulting and Magmatism at Mid-Ocean Ridges, Geophys. Monogr. Ser.*, vol. *106*, edited by W. R. Buck et al., pp. 59–115, AGU, Washington, D. C., doi:10.1029/GM106p0059.

Phipps-Morgan, J., and E. M. Parmentier (1985), Causes and rate-limiting mechanisms of ridge propagation: A fracture mechanics model, *J. Geophys. Res.*, *90*, 8603–8612.

Pollard, D. D., and A. Aydin (1984), Propagation and linkage of oceanic ridge segments, *J. Geophys. Res.*, *89*, 10,017–10,028.

Ross, M. E. (1986), Flow differentiation, phenocryst alignment, and compositional trends within a dolerite dike at Rockport, Massachusetts, *Geol. Soc. Am. Bull.*, *97*, 232–240.

Rubin, A. M. (1995), Propagation of magma-filled cracks, *Ann. Rev. Earth Planet. Sci.*, *23*, 287–336, doi:10.1146/annurev.ea.23.050195.001443.

Rubin, K. H., et al. (2012), Volcanic eruptions in the deep sea, *Oceanography*, *25*(1), 142–157, doi:10.5670/oceanog.2012.12.

Scheirer, D. S., D. J. Fornari, S. E. Humphris, and S. Lerner (2000), High-resolution seafloor mapping using the DSL-120 sonar system: Quantitative assessment of sidescan and phase-bathymetry data from the Lucky Strike segment of the Mid-Atlantic Ridge, *Mar. Geophys. Res.*, *21*, 121–142, doi:10.1023/A:1004701429848.

Sempere, J.-C., and K. C. Macdonald (1986a), Deep-tow studies of the overlapping spreading centers at 9°03′N on the East Pacific Rise, *Tectonics*, *5*, 881–900, doi:10.1029/TC005i006p00881.

Sempere, J.-C., and K. C. Macdonald (1986b), Overlapping spreading centers: Implications from crack growth simulation by the displacement discontinuity method, *Tectonics*, *5*, 151–163.

Sigurdsson, H., and S. R. J. Sparks (1978), Lateral magma flow within rifted Icelandic crust, *Nature*, *274*, 126–130.

Sims, K. W. W., et al. (2002), Chemical and isotopic constraints on the generation and transport of melt beneath the East Pacific Rise, *Geochim. Cosmochim. Acta*, *66*, 3481–3504, doi:10.1016/S0016–7037(02)00909-2.

Sims, K. W. W., et al. (2003), Aberrant youth: Chemical and isotopic constraints on the origin of off-axis lavas from the East Pacific Rise, 9°–10°N, *Geochem. Geophys. Geosyst.*, *4*(10), 8621, doi:10.1029/2002GC000443.

Singh, S. C., et al. (2006), Seismic reflection images of the Moho underlying melt sills at the East Pacific Rise, *Nature*, *442*, 287–290, doi:10.1038/nature04939.

Stewart, M. A., E. M. Klein, and J. A. Karson (2002), The geochemistry of dikes and lavas from the north wall of the Hess Deep Rift: Insights into the four-dimensional character of crustal construction at fast-spreading mid-ocean ridges, *J. Geophys. Res.*, *107*(B10), 2238, doi:10.1029/2001JB000545.

Stewart, M. A., E. M. Klein, J. A. Karson, and J. G. Brophy (2003), Geochemical relationships between dikes and lavas at the Hess Deep Rift: Implications for magma eruptibility, *J. Geophys. Res.*, *108*(B4), 2184, doi:10.1029/2001JB001622.

Stewart, W. K., M. Jiang, and M. Marra (1994), A neural network approach to classification of sidescan sonar imagery from a midocean ridge area, *IEEE Trans. Syst. Man Cybern.*, *19*, 214–224.

Thordarson, T., and G. Larsen (2007), Volcanism in Iceland in historical time: Volcano types, eruption styles and eruptive history, *J. Geodyn.*, *43*, 118–152, doi:10.1016/j.jog.2006.09.005.

Thordarson, T., and S. Self (1993), The Laki (Skaftár Fires) and Grímsvötn eruptions in 1783–1785, *Bull. Volcanol.*, *55*, 233–263, doi:10.1007/BF00624353.

Tong, C. H., et al. (2002), Asymmetric melt sills and upper crustal construction beneath overlapping ridge segments: Implications for the development of melt sills and ridge crests, *Geology*, *30*, 83–86, doi:10.1130/0091-7613.

Tong, C. H., et al. (2003), Influence of enhanced melt supply on upper crustal structure at a mid-ocean ridge discontinuity: A three-dimensional seismic tomographic study of 9°N East Pacific Rise, *J. Geophys. Res.*, *108*(B10), 2464, doi:10.1029/2002JB002163.

Tong, C. H., C. Lana, R. S. White, M. R. Warner, and ARAD Working Group (2005), Subsurface tectonic structure between overlapping mid-ocean ridge segments, *Geology*, *33*, 409–412, doi:10.1130/G21245.1.

Toomey, D. R., D. Jousselin, R. A. Dunn, W. S. D. Wilcock, and R. S. Detrick (2007), Skew of mantle upwelling beneath the East Pacific Rise governs segmentation, *Nature*, *446*, 409–414, doi:10.1038/nature05679.

Wanless, V. D., M. R. Perfit, W. I. Ridley, and E. Klein (2010), Dacite petrogenesis on mid-ocean ridges: Evidence for oceanic crustal melting and assimilation, *J. Petrol.*, *51*, 2377–2410, doi:10.1093/petrology/egq056.

Wanless, V. D., M. R. Perfit, W. I. Ridley, P. J. Wallace, C. B. Grimes, and E. M. Klein (2011), Volatile abundances and oxygen isotopes in basaltic to dacitic lavas on mid-ocean ridges: The role of assimilation at spreading centers, *Chem. Geol.*, *287*, 54–65, doi:10.1016/j.chemgeo.2011.05.017.

Wanless, V. D., M. R. Perfit, E. M. Klein, S. White, and W. I. Ridley (2012), Reconciling geochemical and geophysical observations of magma supply and melt distribution at the 9°N overlapping spreading center, East Pacific Rise, *Geochem. Geophys. Geosyst.*, *13*, Q11005, doi:10.1029/2012GC004168.

Waters, C. L., K. W. W. Sims, E. M. Klein, S. M. White, M. K. Reagan, and G. Girard (2013), Sill to surface: Linking young off-axis volcanism with subsurface melt at the overlapping spreading center at 9°03′N East Pacific Rise, *Earth Planet. Sci. Lett.*, *369–370*, 59–70, doi:10.1016/j.epsl.2013.03.006.

White, S. M., R. M. Haymon, D. J. Fornari, M. R. Perfit, and K. C. Macdonald (2002), Correlation between volcanic and tectonic segmentation of fast-spreading ridges: Evidence from volcanic structures and lava flow morphology on the East Pacific Rise at 9°–10°N, *J. Geophys. Res.*, *107*(B8), 2173, doi:10.1029/2001JB000571.

White, S. M., R. M. Haymon, and S. Carbotte (2006), A new view of ridge segmentation and near-axis volcanism at the East Pacific Rise, 8–12°N, from EM300 multibeam bathymetry, *Geochem. Geophys. Geosyst.*, *7*, Q12O05, doi:10.1029/2006GC001407.

White, S. M., J. L. Mason, K. C. Macdonald, M. R. Perfit, V. D. Wanless, and E. M. Klein (2009), Significance of widespread low effusion rate eruptions over the past two million years for delivery of magma to the overlapping spreading centers at 9°N East Pacific Rise, *Earth Planet. Sci. Lett.*, *280*, 175–184, doi:10.1016/j.epsl.2009.01.030.

Wright, T. J., C. Ebinger, J. Biggs, A. Ayele, G. Yirgu, D. Keir, and A. Stork (2006), Magma-maintained rift segmentation at continental rupture in the 2005 Afar dyking episode, *Nature*, *442*, 291–294, doi:10.1038/nature04978.

Zaino, A., E. Klein, D. Wanless, W. I. Ridley, S. M. White, M. Perfit, A. Nunnery, and Anonymous (2008), Phenocryst abundances and compositions at the 9deg 03′N overlapping spreading center: Implications for magma source composition, *Eos Trans. AGU*, *89*(53), *Fall Meet. Suppl.*, Abstract V41B-2085.

Zindler, A., H. Staudigel, and R. Batiza (1984), Isotope and trace element geochemistry of young Pacific seamounts: Implications for the scale of upper mantle heterogeneity, *Earth Planet. Sci. Lett.*, *70*, 175–195.

Zurevinski, S. E., and R. H. Mitchell (2011), Highly evolved hypabyssal kimberlite sills from Wemindji, Quebec, Canada: Insights into the process of flow differentiation in kimberlite magmas, *Contrib. Mineral. Petrol.*, *161*, 765–776, doi:10.1007/s00410-010-0561-8.